Surveys in Geophysics
https://doi.org/10.1007/s10712-023-09812-w

Impact of Source Modelling and Poroelastic Models on Numerical Modelling of Unconsolidated Granular Media: Application at the Laboratory Scale

K. Asfour[1] · R. Martin[1] · D. El Baz[2] · L. Bodet[3] · B. Plazolles[1]

Received: 17 February 2023 / Accepted: 3 October 2023
© The Author(s), under exclusive licence to Springer Nature B.V. 2023

Abstract
The near surface is characterized by using different numerical techniques, among them seismic techniques that are non-destructive. More particularly, for a better understanding of acoustic and seismic measurements in unconsolidated granular media that can constitute the near surface, many studies have been conducted in situ and also at the laboratory scale where theoretical models have been developed. In this article, we want to model such granular media that are difficult to characterize. At the laboratory scale, dry granular media can be modelled with a homogenized power-law elastic model that depends on depth. In this context, we validate numerically a similar power-law elastic model for such media by applying it to a homogenized elastic medium or to the solid frame of a poroelastic medium that consists of solid and air components. By comparing the response of both rheologies, we want to highlight what poroelastic media can bring to better reproduce the experimental data in the time and frequency domains. To achieve this objective, we revisit studies carried out on unconsolidated granular media at the laboratory scale and we compare different models with different rheologies (elastic or poroelastic), dimensions (2D or 3D), boundary conditions (perfectly matched layer/PML, or Dirichlet) and locations of the source (modelled as a vibratory stick or a point force) in order to reproduce the experimental data. We show here that a poroelastic model describes better the amplitudes of the seismograms. Furthermore, we study the sensitivity of the seismic data to the source location, which is crucial to improve the amplitude of the signals and the detection of the different seismic modes.

Keywords Porous and granular media · Wave propagation · Numerical modelling · Dispersion analysis · Surface waves

Article Highlights

- We perform a numerical characterization of unconsolidated granular dry media using elastic and poroelastic homogenized models and numerical modelling of 2D/3D elastic waves and 2D poroelastic waves

Extended author information available on the last page of the article

- We add numerically a better source of excitation of the medium to improve and better reproduce amplitudes of surface waves and velocity phase dispersion curves
- Dispersion analysis gives better wave mode descriptions between numerical and experimental/read data at the laboratory scale

1 Introduction

A natural medium can be composed of unconsolidated materials such as clay, silt, sand, gravel or materials derived from the erosion of rocks. It is thus important to characterize media made of these materials to better understand acoustic and seismic measurements in such soils and their related geological environments. This point is particularly important in the case of near-surface studies, which feature complex environment that can contain natural resources such as water, gas, and hydrocarbons. More generally, it is interesting to study the near surface because it is the place of fluid exchanges and life activities as well as the interface for earth–atmosphere coupling.

Many studies on elastic wave velocities in unconsolidated materials have been conducted in situ and at the laboratory scale, and theoretical models have been proposed. In particular, in the case of granular media studies, new theoretical and numerical models have been designed those last years for acoustic characterization and response studies of meta-materials, porous and granular media at the laboratory scale by Palermo et al. (2018); Zaccherini et al. (2020); Pu et al. (2020). Among the seismic techniques used to determine the physical properties of such media, we can cite the tomography techniques that are based on minimizing the first arrival time residuals (Zelt and Smith 1992; Le Meur 1994; Improta et al. 2002; Ravaut 2003) or the MASW (multiple analysis of surface waves) technique (Nazarian and Stokoe 1984; Ganji et al. 1997; Park and Elrick 1998; Xia et al. 1999; Foti 2000; Bitri et al. 2002; Xia 2014) which studies the surface wave dispersion. Toolboxes like SWIP (Surface-Wave Inversion and Profiling method), presented in Pasquet and Bodet 2017, can be used to estimate the S-shear wave velocities (V_s) of such media. Some common resulting models proposed at the near-surface scale show an important increase in P and S wave velocity as a function of depth. Indeed, based on Hertz–Mindlin contact theory (in the context of intergrain forces modelling), the velocity structure of such media can be modelled as (Gassmann 1951): $V_{p,s} = \gamma_{p,s}(\rho g z)^{\alpha_{p,s}}$, where g is the gravity acceleration, ρ is the bulk density of grains or glass beads, $\gamma_{p,s}$ is a depth-independent coefficient, which mainly depends on the elastic properties of the grains, porosity and coordination number of the packed structure, and $\alpha_{p,s}$ is the power-law exponent. The parameter $\alpha_{p,s}$ depends on the grain dispersion, grain disorder, grain contacts and the form of grains (Makse et al. 1999; Zimmer et al. 2007; Tournat and Gusev 2010; Schön 2015). In those studies, similar power-law profiles of seismic wave velocities have been investigated. This power-law exponent is generally close to 1/6 for random close packing of uniform spheres. A similar exponent value has been proposed by Bachrach et al. (1998) for a shallow sand medium in situ. However, in real materials strong contact disorders between grains can be present due to low degrees of heterogeneity in grain sizes or sphericity, and then, this exponent coefficient can be different from 1/6. This exponent is not only dependent on the dispersion of grain size or grain sphericity, but it depends also strongly on the confinement pressure of the medium. In many experiments, this exponent can be increased for lower static pressures applied to the medium (0.1 - 200 kPa) and can reach values from 1/6 up to 1/4.

In this context, before characterizing any (partially or fully) saturated media with fluid (water, gas), we want to model correctly the seismic wave propagation in unconsolidated

granular media in the dry regime. In particular, we revisit here the study in Bodet et al. (2014) at the laboratory scale for granular media (made of glass beads) that are submitted to low pressures and do not contain any fluid. The physical model deduced is a power-law model with $\alpha_{p,s}$ close to $\frac{1}{3}$, which is a typical value that can be reached in the experiments in the case of very low pressures (less than 0.1 kPa). Besides, for this range of low pressures, similar exponent coefficients have been obtained in other acoustic experiments by Jacob et al. 2008; Tournat and Gusev 2010. However, we want here to perform a deeper acoustic signal analysis in this context for different numerical designs in 3D and 2D to accelerate the computations and to model the relevant signals without noise and without reflections contaminating the computational domain. More particularly, we compare different rheological (elastic or poroelastic) models involving our power-law and we investigate their ability to better reproduce the seismograms and phase dispersion diagrams for the granular medium under study. On the medium/long term, all the methodology used here could be applied at the laboratory scale and also to data collected at near-surface field (in situ) scales.

The main objective of this study is to numerically validate the models considered by verifying whether they allow us to better interpret the data recorded in the laboratory. In order to do this, numerical simulations are run to fully replicate the configuration of the laboratory experiments. The physical problem consists in solving the seismic wave equation for different rheologies (pure elastic, poroelastic) in dry regime in order to determine which of them best explains the laboratory data. Besides, in a previous work (Bodet et al. 2014) significant differences in amplitude between the experimental and simulated waveforms were exhibited and we thus identified two main issues to address in order to better model physically and numerically this kind of complex granular medium:

- Finding a more adequate rheological law (elastic or poroelastic) describing the mechanical behaviour of the medium.
- Studying the impact of the type of source wavelet on the computed data by modelling the source as a vibratory stick, as in the experiment of Bodet et al. (2014) or as a virtual point source located at different depths.

Indeed, the choice of the rheological law and the source model influence the waveforms and the amplitudes as well as the different surface and P-modes in the dispersion diagrams. This will be discussed in the following sections of this study.

First, to simulate such media, 3D numerical elastic wave propagation simulations are performed in the case of a pure elastic medium. The calculated solutions are then compared with experimental data recorded at the laboratory scale. Time and frequency (dispersion) analyses are done to compare, respectively, the first arrivals and the dispersion curves of the experimental data with the simulated ones.

Second, since the physical model considered is vertically stratified and invariant in the direction orthogonal to the vertical plane containing the source and the line of receivers, we can reduce the 3D model to a 2D one. The 2D calculated seismograms can reproduce the 3D ones by introducing a source–receiver distance rescaling of the real data seismograms following a similar approach as in Forbriger et al. (2014). Besides, the 2D computations allow us also to accelerate even more the calculations. The introduction of the 2D calculations is relevant because the source injects the maximum of energy into the vertical plane it belongs to and the model is invariant in the orthogonal direction. Furthermore, since the 3D waves are attenuated due to the geometrical divergence and since the vertical walls of the experimental box are far enough from the seismic line, the only

significant acoustic reflections are coming from the bottom of the box. This is another reason of performing 2D simulations in the vertical plane. Therefore, we study different configurations in 3D and 2D with a free surface on top and compare the results to the real data. In some cases, we apply efficient perfectly matched layer (PML) absorbing boundary conditions to all vertical walls in presence or not of Dirichlet conditions at the bottom. The introduction of the PMLs allows us to truncate the computational domain and to also reduce the computing time while reproducing the experimental data and keeping the relevant acoustic phases and modes we are interested in.

Third, we make the rheology more complex (porous medium using a Biot poroelastic model for instance) in 2D to compare it to the homogenized elastic medium and to the experimental results.

Comparisons between simulated and experimental data are done in two domains:

- Time domain: we detect the first travel-time arrivals of the seismic waves.
- Frequency domain: we calculate the dispersion curves using a slant–stack transform.

The choice of the numerical tools was made taking into account four main criteria: accuracy, performance, simplicity of the method, and the nature of the physical problem to be solved. A 3D finite difference code, fourth-order in space and second-order in time, called UNISOLVER (updated version of the 3D SEISMIC_CPML code (Komatitsch and Martin 2007; Martin and Komatitsch 2009; Martin et al. 2010)) is used here to solve the wave equations in a stratified elastic medium taking into account different models and computational configurations involving strong depth gradient velocities. The fourth-order finite difference discretization in space is a good choice because in the case of a flat topography, it is sufficiently accurate, easy to implement and faster than other numerical methods. Mirror conditions are implemented at the free surface. With this type of boundary conditions, the numerical solution is sufficiently accurate at the free surface and in the inner computational domain. For more details, the reader is referred to the work on fourth-order finite differences of Graves (1996) and Moczo et al. (1997, 2010, 2001) for 3D elastic and viscoelastic modelling, respectively. Optimized Perfectly Matched Layer/PML absorbing (Komatitsch and Martin 2007; Martin et al. 2008b) and free surface conditions are implemented and validated by comparing with reference codes such as SPECFEM (spectral finite elements, Komatitsch (1997)), which is commonly used in the geophysical community. UNISOLVER is parallelized, and therefore, the computation time is reduced, which makes it very efficient for the realization of our numerical simulations. In the present study, we extend the discretization to the 2D and 3D poroelastic media (see also Bodet et al. (2014)). 2D versions of this code for both elastic and porous media are also used to highlight the contribution of the porous medium to the elastic medium, and also the ability of the poroelastic model to better reproduce the acoustic modes in the frequency domain.

The structure of this paper is summarized as follows: Section 2 deals with the experimental setup and the physical homogenized elastic model obtained by inversion of first arrivals and dispersion diagrams. In Sect. 3, the numerical setup for the different rheological models is given. In Sects. 4 and 5, qualitative (seismograms, spectrograms and dispersion images) and quantitative (first arrivals, dispersion curves) analyses are done on the different numerical models considered, respectively. In Sect. 6, we consider different locations of the numerically modelled sources to show the influence of the choice of the source location at depth on the detection of the different seismic modes. Finally, the results obtained are discussed. In Sect. 7, conclusions, recommendations, and future work are presented.

2 Experimental Setup and Physical Model

2.1 Experimental Setup

In this paper, we are interested in experiments on unconsolidated granular media, which are carried out at the laboratory scale (see Bodet et al. (2014)). The studied physical medium has a length of 1 m, a height of 0.22 m and a width of 0.8 m. The box is filled with 180–300- μm -diameter glass beads (GB1), and the bottom of the box consists of a metallic sieve glued on a perforated plate (see Fig. 1). The deposition process has been done experimentally to ensure a homogeneous distribution of the glass beads. The bulk density has been measured many times during the deposition process, and it was always estimated in a range between 1600 and 1610 kg/m^3. We thus make the choice to consider a density value of 1610 kg/m^3 for the bulk density ρ_{GB1} which is the most representative, and its corresponding porosity is $\Phi_{GB1} = 0.356$.

The source consists of a metal stick connected to a waveform generator (see Fig. 2) with a dominant frequency $f_0 = 1500\ Hz$. The latter is injected in the vertical yOz-plane with a tilted angle of 20^o with the vertical normal to the free surface.

For a given source location, the normal component of the particle velocity (V_z) is recorded in time at the surface of the medium as a "seismogram" using an oscilloscope. Up to 100 traces were recorded (using an oscilloscope) with a sampling rate of 10^{-5}s (0.01ms) over a time-series length of 50 ms in linear single-channel walkway mode along the Oy direction.

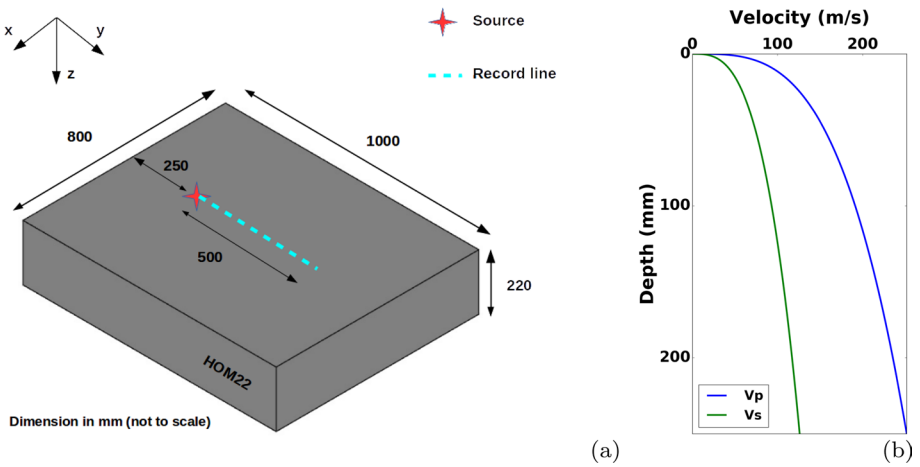

Fig. 1 **a** Physical model (PM) in Bodet et al. (2014): a granular layer 180–300- $\times 10^{-6}$ m-diameter GBs (GB1) sieved into a $(1000 \times 800 \times 220)$. 10^{-3} m box. The bottom of the box consisted of a metallic sieve (dashed lines) glued to a perforated plate. The PM HOM22 was prepared by sieving GB1 directly onto the metallic sieve. We consider a density value of 1610 kg/m^3 for the bulk density ρ_{GB1} which is the most representative. This value led to a porosity of $\Phi_{GB1} = 0.356$. (x_s, y_s)= $(0.4m, 0.25m)$ are the source location coordinates (marked by a red star at 25 cm from left wall), and the dashed light blue line shows the data recording line (50cm long from the source) and acquisition parameters. **b** The power-law model for the dry unconsolidated granular medium case (zero overpressure) using parameters $\alpha_{p,s}$ and $\gamma_{p,s}$ estimated by simulated annealing-based inversion of the measured first arrival times for V_p and of the dispersion curve related to the fundamental (Rayleigh) mode for V_s extracted from the dispersion diagrams

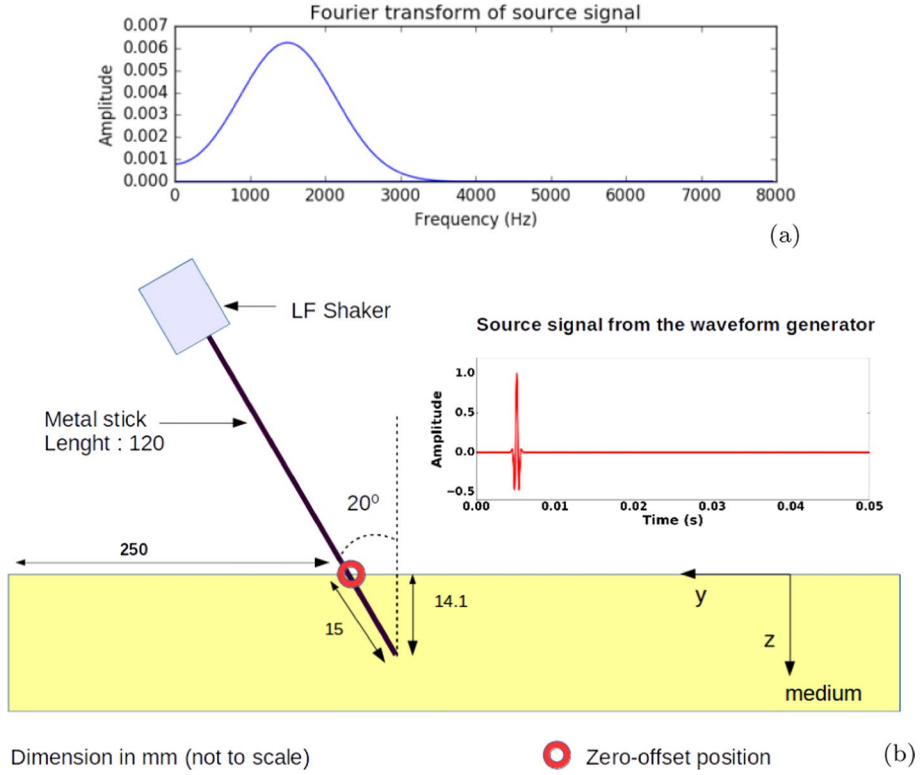

Fig. 2 The force source signal is sent from a waveform generator to a low-frequency (LF) shaker exciting a 120-mm metal stick buried in the granular material over a 15-mm length. The laser beam is set at the zero-offset position (0.25 *m* in the length direction) to record the vertical component of velocity V_z of the stick (the red line in the right inset). **a** Source signal spectrum centred on 1500 *Hz*; **b** detail of vibrator source and source signal configuration

2.2 Experimental Data

The experimental data at our disposal have been recorded at 25 receivers placed linearly and equidistantly at the surface of the medium. For a given source location, the normal component of the particle velocity (V_z) is recorded in time at the surface of the medium as a "seismogram" using an oscilloscope at a sampling time rate of 0.01ms. From the source over a length of 0.5 *m* in the *y*-direction, the spacing between the receivers is 0.02 *m*.

We underline that here the data are not normalized data. However, if the data are normalized with respect to the maximum of the signals measured over all receivers, then source ringing effects appear at the source location and also at near offset as observed in Jacob et al. (2008); Bodet et al. (2010); Bergamo et al. (2014); Bodet et al. (2014). According to these authors, it is very hard to remove them. A better design of the contact between the source and the beads should be proposed to reduce or eliminate those effects. In the following sections, we thus concentrate our analysis on the main relevant signal. To reduce the source effects and noise, we consider the receivers located 5 cm away from the source and we filter the data with a Butterworth band-pass filter in the 100–3000 *Hz* frequency band since the signal amplitude is maximal in this window, as shown in Fig. 3. Besides,

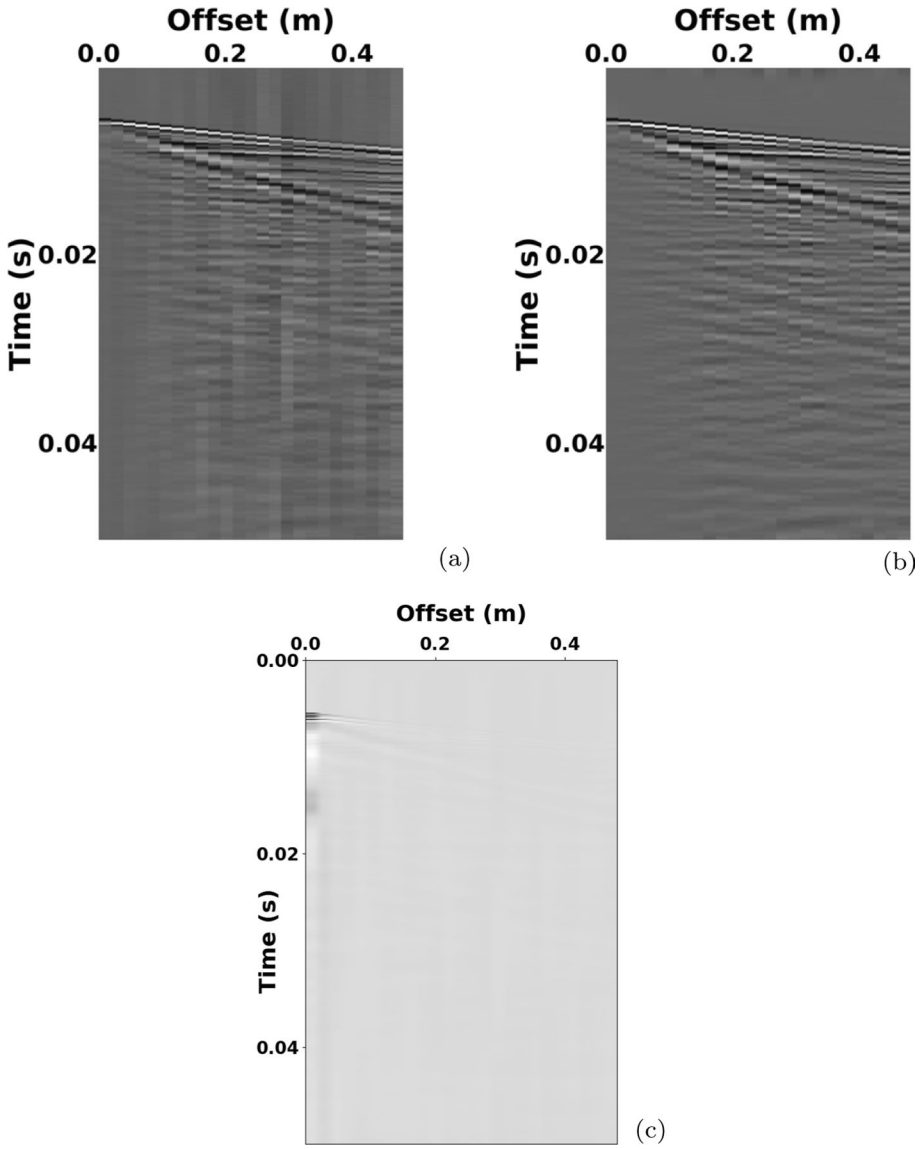

Fig. 3 Experimental data not filtered (**a**) and filtered (**b**) , as well as their difference (**c**). Time is given in seconds

in Fig. 3c the difference between non-filtered and filtered data exhibits some small noise effects close to the source due to the ringing effects mentioned before. In Fig. 4, we show the seismograms of V_z component (filtered and not filtered) at receivers 10, 15 and 20 located at 20, 30 and 40 *cm* from the source, respectively. In Figs. 3 and 4, the non-filtered and filtered data are both showing the same acoustic phases in presence of noise or not, and their difference only shows some coherent noise. In the following sections, we will thus only compare solutions with filtered real data.

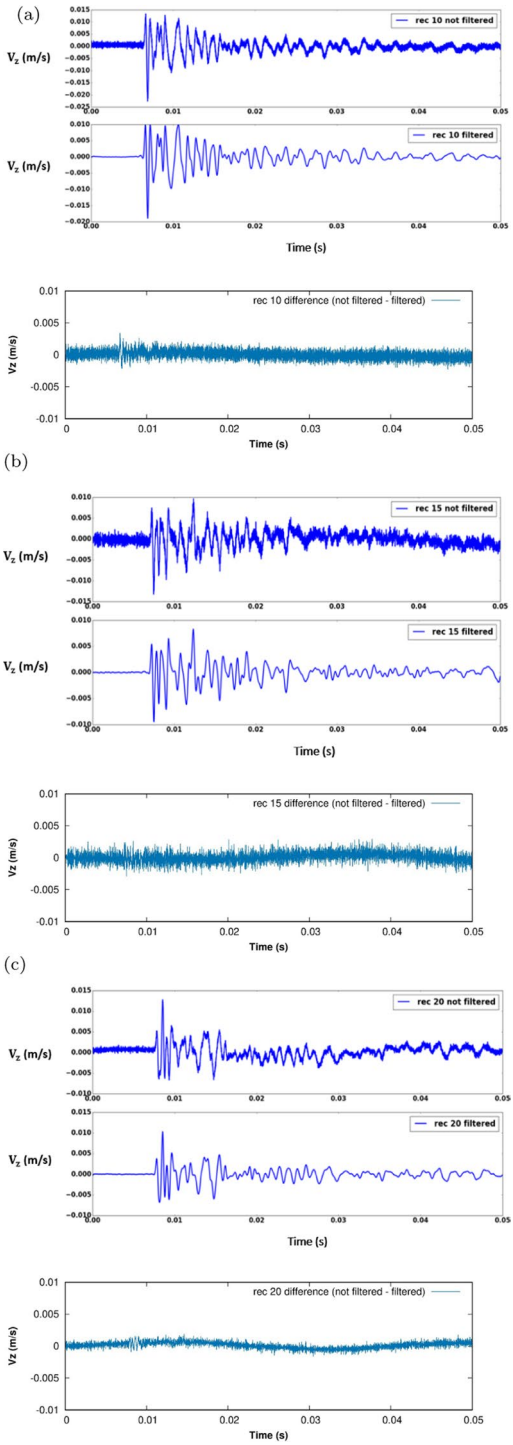

Fig. 4 Experimental traces representing the normal component of particle velocity (Vz) not filtered and filtered as well as their difference (noise) at receivers 10 (**a**), 15 (**b**) and 20 (**c**), respectively

Due to the fact that we aim at studying 2D seismograms because (1) the model is vertically 2D and invariant according to the direction orthogonal to the vertical plane, and (2) the 2D cases are much faster to compute than the 3D case, it is crucial to transform the real data from 3D to 2D and to model the source in the synthetic cases for the current model under study. In the close vicinity of the source, the wavefield transformation from 3D to 2D scales as $\sqrt{rV_{ph}}$ where r is the offset and V_{ph} is the phase velocity. But for larger offsets r from the source, the medium is dispersive and the amplitude of the signals is scaling as $r/\sqrt{t}$. In a given frequency band, the real data seismograms are convolved with $1/\sqrt{t}$ and are scaled respect to the offset as previously mentioned and proposed by Schäfer et al. (2012); Groos et al. (2013, 2014a) and also very well synthetized in Forbriger et al. (2014). Those corrections have been applied efficiently in near-surface applications in the context of full-waveform inversion in presence or not of attenuation as in Schäfer et al. (2013, 2014); Groos et al. (2014b).

2.3 Physical Model

We are interested in a V_p/V_s model obtained from the experiment on an unconsolidated granular medium as in Bodet et al. (2014). The latter is deduced by ray tracing-based travel-time inversion for the V_p model and phase velocity diagram inversion for the V_s model. Those inverted V_p and V_s models are given by a power-law dependent on hydrostatic pressure as proposed in Gassmann (1951) (Fig. 1b):

$$V_p = \gamma_p(\rho g h)^{\alpha_p} \tag{1a}$$

$$V_s = \gamma_s(\rho g h)^{\alpha_s} \tag{1b}$$

where ρ, g and h are, respectively, the density, the gravitational acceleration at Earth surface ($g = 9.81\, m.s^{-2}$) and the depth of the medium. The parameters γ and α for the dry case are estimated by simulated annealing-based inversion of the measured first arrival times for V_p and of the dispersion curve related to the fundamental (Rayleigh) mode for V_s. Those inverted γ and α parameters have the following values: $\alpha_p = 0.3$, $\gamma_p = 21$, $\alpha_s = 0.33$ and $\gamma_s = 8.2$ (see Bodet et al. (2014)).

In Bodet et al. (2014), this model was partially validated numerically using a 3D elastic finite difference code. But there was still a problem in reproducing the amplitudes of higher modes. In the seismograms as well as in the velocity phase dispersion diagrams, the computed amplitudes were too high when compared to the real data. To mitigate this drawback, first, we reproduce the results of Bodet et al. (2014) with our 3D finite difference code UNISOLVER. Secondly, we reduce the 3D model to a 2D model to accelerate the computations, and finally, we integrate the V_p/V_s model into a 2D poroelastic model according to the Biot poroelastic model (Biot 1956a), which makes the assumption of interconnected pores between grains and enables to describe and take into account medium wavelengths of the two-component porous medium. One of the main goals is to increase the complexity of the rheologies to better reproduce the amplitudes of higher modes.

3 Numerical Setup

We consider the following three models (the reader is referred to appendices A, B and C for elastic and poroelastic equations):

- 3D elastic: we use UNISOLVER (our finite difference/FD code which is fourth-order in space and second-order in time) (Komatitsch and Martin 2007) to reproduce the results of Bodet et al. (2014).
- 2D elastic: we reduce the 3D model to the vertical plane where the metal stick is located. In this case, we use our FD code seismic_CPML_elastic (fourth-order in space and second-order in time) (Komatitsch and Martin 2007), and we compare the results to the experimental data.
- 2D poroelastic: poroelastic materials are most of the time modelled using the Biot theory (Biot 1956a, b). In this study, we choose to remain in the context of Biot models. Thus, we take into account parameters such as porosity, permeability, viscosity and tortuosity (measured during the experiment). The compressional P wave velocities (fast and slow) and the effective shear S wave velocities in the porous medium depend also on the P and S elastic wave velocities of the solid frame that is modelled in our present study using equation (1). A version of Seismic_CPML for Biot model is used (Martin et al. 2008b).

For each model, we consider three cases corresponding to three different types of boundary conditions:

- (*Case 1)* Dirichlet: in this case, all the boundaries except the free surface are Dirichlet boundary conditions (i.e., particle velocities equal to zero); Dirichlet conditions are defined to simulate a rigid material on the five other sides of the box in 3D, and on the three other sides in 2D.
- (*Case 2)* PMLs: in this case, we consider absorbing boundary conditions (C-PMLs) on all the boundaries except the free surface and the bottom boundary where a Dirichlet condition is applied. The PMLs allow to absorb the outgoing waves to mimic an open medium.
- (*Case 3)* Full PMLs: in this case, on all the boundaries except the free surface, absorbing boundary conditions (C-PMLs) are considered.

In all cases, the free surface condition is implemented at the top of the computational domain using the zero normal traction assumption for the different cases.

For the different models and cases, the force source signal (see Figs. 5 and 6) is injected all along the metal stick. The latter is simulated numerically by injecting the time wavelet source signal over a series of points located along the stick.

3.1 3D/2D Elastic Models

The physical model has a width of 0.35 m, a length of 1 m and a height of 0.215 m. The density is given by $\rho = 1610\, kg/m^3$.

In 3D, we consider a uniform mesh such that $\Delta X = \Delta Y = \Delta Z = 5.\ 10^{-4} m$ and composed of $70 \times 2000 \times 430$ points. The total number of points of the mesh is 60,2 million points. The time step used is $\Delta t = 10^{-6} s$, and the total number of time steps is 50000 corresponding to 50 ms (time period of the experiment). In this case, the Courant–Friedrichs–Lewy/CFL stability number is equal to 0.6. In our simulations, the injected source is the real (experiment) source time wavelet (sampling rate of 10^{-5} s) interpolated at the simulation time step Δt. The spectrum of the source is centred around a dominant frequency of 1500 Hz (see Fig. 2a).

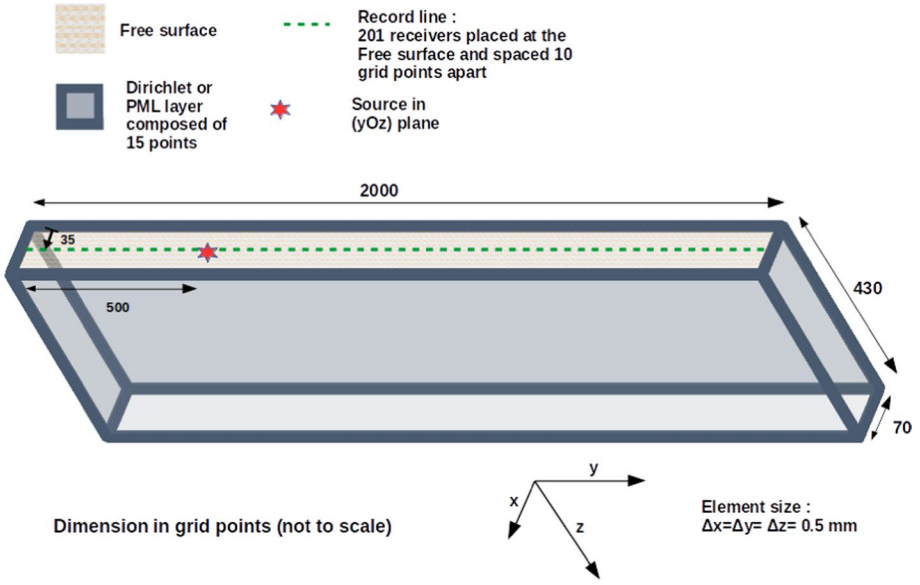

Fig. 5 The 3D numerical model is discretized by elements of 5×10^{-4} m in each direction of space for a mesh of $70 \times 2000 \times 430$ points (0.35 $m \times 1$ $m \times 0.215$ m). Dirichlet conditions (case 1) or absorbing PML layers composed of 15 points each (cases 2 and 3, i.e., PMLs or full PMLs) are applied on the outer boundaries except at the free surface. The free surface is defined at the top of the computational domain. The force source (in red) is implemented with an angle of 20^o from the normal to the free surface, to meet the experimental configuration (see the 2D numerical setup in Fig. 6). The receivers (dashed line in green) are spaced every 5×10^{-3} m (10 grid points) at the free surface

PML layers are composed of 15 points for efficient boundary absorption. The V_p and V_s modelled velocities are invariant in the direction orthogonal to the vertical plane and follow the power-law trend with depth (see Fig. 1b). The velocity profiles, continuous in theory, are discretized according to the spacing discretization ΔZ in depth.

The receivers are spaced every $5\,10^{-3}$ m (10 grid points) at the free surface to record the seismograms of the normal component of the particle velocity (see Fig. 5).

We reduce the 3D model to a 2D model by considering only the vertical plane where the metal stick (source) is located.

In order to obtain amplitudes and waveforms of the recorded signals as close as possible to the experimental data, we simulate different configurations using the 3D parallel FD code UNISOLVER (we refer the reader to appendix D for code performance details): with Dirichlet (case 1), PMLs (case 2, just at the four vertical outer boundary walls and Dirichlet at the bottom) or full PMLs (case 3, PML layers everywhere) conditions except at the free surface. In the 2D case, we consider the same configurations mentioned above and we also use the 2D code seismic_CPML_elastic.

3.2 2D Poroelastic Model

In the poroelastic case (see appendix C for the Biot model used here), one considers the same discretization in space and time as in the elastic cases. The length and width of the box are also preserved.

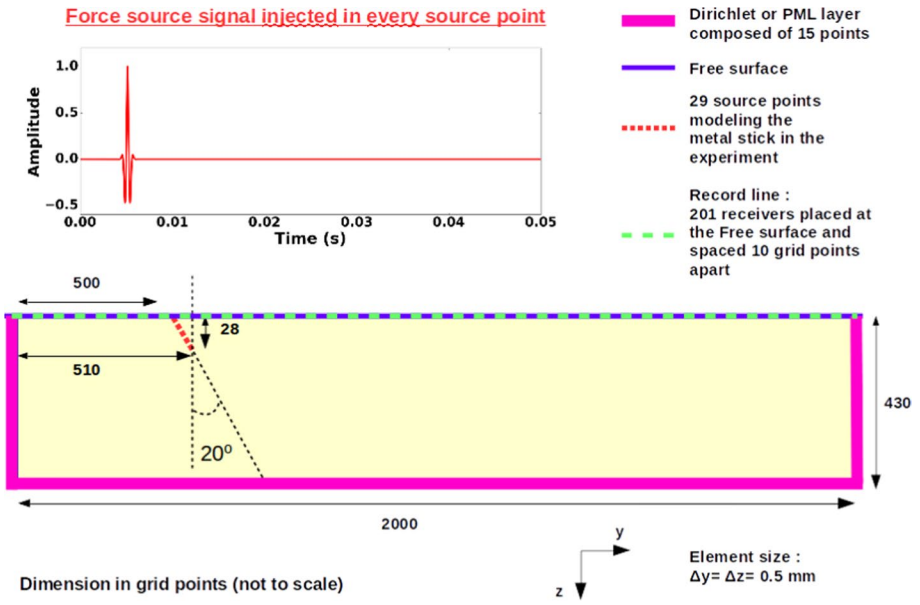

Fig. 6 The 2D numerical model is discretized by elements of $5.10^{-4}m \times 5.10^{-4}m$ for a mesh of 2000×430 points ($1\,m \times 0.215m$). Absorbing PML layers composed of 15 points each one or Dirichlet conditions are applied to the outer boundaries except at the free surface which is defined at the top of the computational domain. The force source (in red) is implemented with an angle of 20^o from the normal to the free surface and injected at every source point along the stick length, to meet the experimental configuration and the stick form. The receivers (dashed line in green) are spaced every $5 \times 10^{-3}m$ (10 grid points) at the free surface

In our simulation, the solid components are glass beads and the fluid considered is the air. The density of the solid $\rho_s = 2500\ kg/m^3$ and the density of the fluid $\rho_f = 1.20\ kg/m^3$ give an apparent density $\rho_w = 6,46\ kg/m^3$ and a density of the saturated medium $\rho = 1610\ kg/m^3$ (using relations in the Biot model). The porosity, the permeability, the viscosity and the tortuosity are given by $\Phi_{GB} = 0.356$, $\mathcal{K} = 9.510^{-11}\ m^2$, $\nu = 1.907 \cdot 10^{-5}$ Pa.s and $a = 1.91$, respectively.

The bulk modulus of air is 0.101 MPa, and the bulk modulus of the solid and saturated medium is computed depending on the variation of P-wave and S-wave velocities, which affect the effective Lamé parameters λ and μ of the porous medium and λ_s of the solid frame (see Fig. 7 for the different velocities computed with this model). Seismic velocities V_s and V_p characterize the pure elastic model, while V_s, V_{PFAST} and V_{PSLOW} characterize the porous medium. The difference between the poroelastic and elastic V_s velocities is very small and is thus multiplied by 10^3 to see it more clearly. S-wave velocity is similar for both the elastic and the poroelastic models because the fluid represented by the air presents very low shear stress compared to the solid frame or even no-shear stress (as any other fluid). Its contribution is thus introduced essentially through the bulk compressional stress. Therefore, the fluid is essentially contributing to pressure and V_p (fast and slow) velocities. We use seismic_CPML_poroelastic, a FD code (fourth-order in space and second-order in time) to resolve the 2D Biot model in the different boundary cases considered.

When we calculate the maximum frequency of the source $f_{max} = \pi f_0$ and the cut-off frequency f_c (see eq. (27) in appendix C), we obtain: $f_{max} = 4710\ Hz < f_c = 4959.592\ Hz$

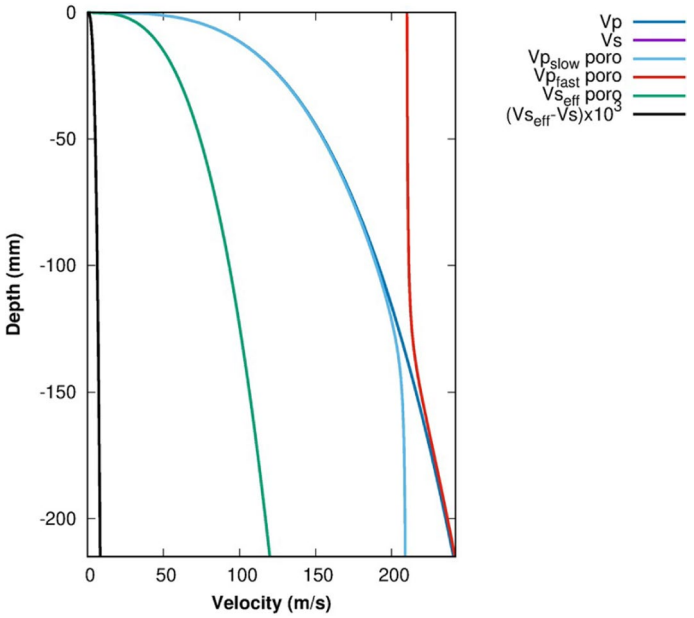

Fig. 7 The different velocities computed for the elastic (V_s and V_p) and poroelastic (V_{seff}, V_{pFAST} and V_{pSLOW}) models. The difference between the poroelastic and elastic shear velocities is very small and is thus multiplied by 10^3 to see it more clearly

which means that we can consider a Biot model without attenuation (the reader is referred to Morency et al. (2009) for more details).

4 Qualitative Analysis

4.1 Seismograms and Spectrograms

In Fig. 8a, the experimental seismograms are shown. The directivity of the source is located in the vertical plane (*yz*) and along the longitudinal length *y*. The source injects essentially the energy in the vertical *(yz)* plane containing the line of receivers. The waves propagating in the perpendicular direction (plane *xz*) have smaller amplitudes than those propagating in the (*yz*) plane, and spend more time compared to the *yz*-plane waves to reach the vertical walls located far from the source axis and to come back to the receivers as observed by Jacob et al. (2008); Bergamo et al. (2014); Bodet et al. (2014). The amplitudes of these waves are thus strongly attenuated before reaching the receivers. The only main reflections that can be observed are coming from the bottom of the box. This is the reason why we apply PML absorbing layers in the 2 vertical planes (*xz*) parallel and far from the longitudinal line of receivers. This allows to reduce significantly the computational time in 3D configurations. However, it is important to study 3D different cases with 1) pure Dirichlet conditions (case 1) applied at all vertical walls and bottom of the box, 2) PMLs at all vertical walls except at the bottom (case 2) or 3) full PMLs at all walls

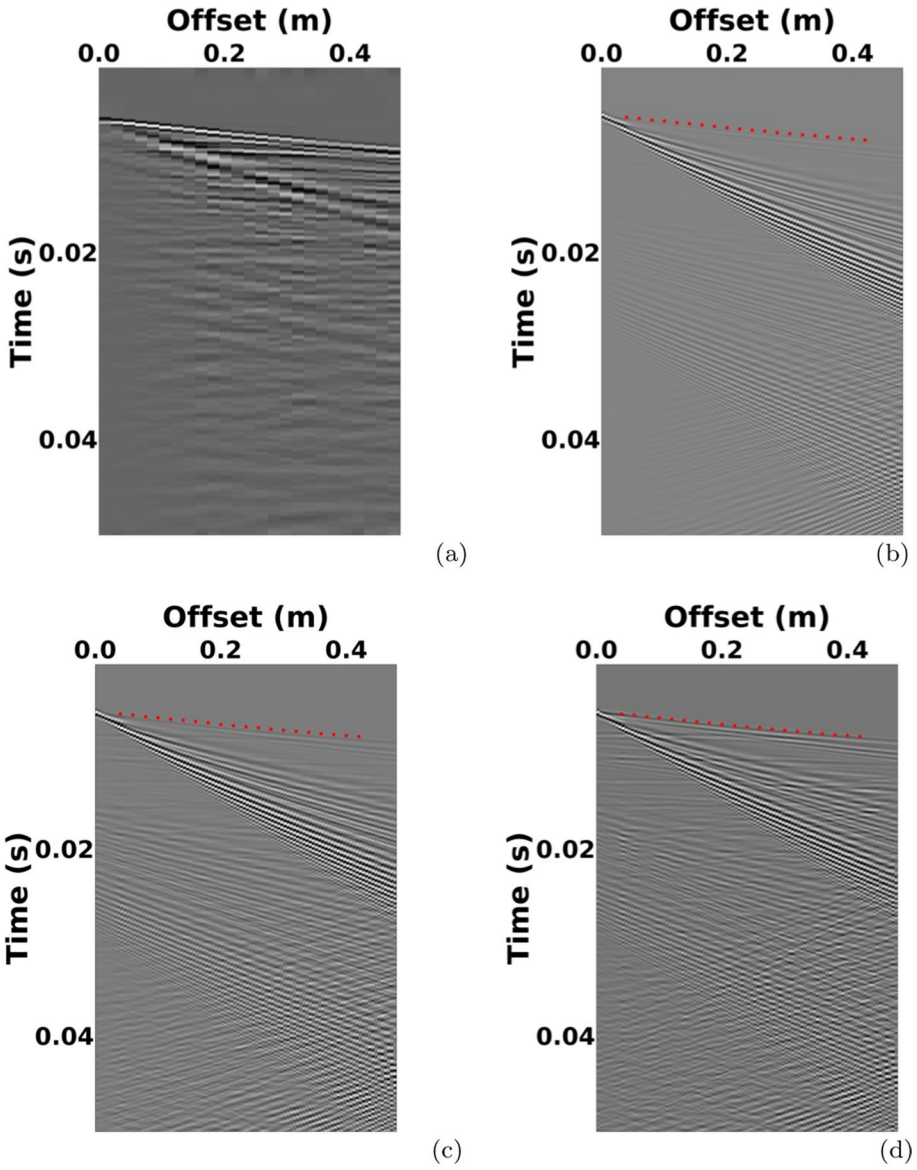

Fig. 8 Comparison between experimental filtered (**a**), 3D elastic (**b**), 2D elastic (**c**) and 2D poroelastic (**d**) seismograms (vertical component of particle velocity) in the Dirichlet case

(case 3). This allows us to exhibit and identify the signals of interest and filter part of the signals reflected back from the walls, to concentrate our efforts on the relevant signals and to evaluate whether 2D simulations can reproduce the seismograms instead of using 3D simulations.

Figure 8 shows also the numerical seismograms for the different models (3D elastic, 2D elastic and 2D poroelastic) in the Dirichlet case. We can clearly see the P-wave followed

by a train of guided waves of the P-SV type. The P-wave, itself guided by the gradient of mechanical properties of the medium, corresponds to fast modes considered as essentially longitudinal. We can also see the reflections of the waves on the boundaries due to the considered Dirichlet conditions (case 1). However, in the PMLs and full PMLs (cases 2 and 3 respectively) cases, these reflections disappear (see Figs. 9 and 10). In Fig. 9 corresponding to case 2, the horizontal events are appearing in the 2D elastic and 2D poroelastic cases due to the reflection of the waves at the Dirichlet bottom boundary. However, no such horizontal events are appearing in the 3D elastic case because of the attenuation of the waves amplitudes due to 3D geometrical divergence attenuation. To avoid such reflections in the 2D elastic and poroelastic simulations and to be coherent with the non-reflecting waves of the 3D case 2, we will apply full PMLs (case 3) in the 2D simulations. In the spectrograms, in the case of Dirichlet conditions, the reflections contaminate the frequency signal (see Fig. 11). Imposing absorbing conditions (C-PML) at the outer boundaries absorbs the reflections and makes the spectrogram clearer (see Figs. 12 and 13). By comparing the PMLs and full PMLs cases, one notices that the Dirichlet conditions imposed at the bottom of the medium in the PMLs case (case 2) create interferences represented by horizontal lines.

Therefore, in the next sections, we will thus continue our analyses by considering only the full PMLs case in which no reflections are coming back into the computational domain.

4.2 Dispersion Images

As in Park and Elrick (1998), a slant–stack transform (an oblique summation of normalized signal amplitudes in the frequency domain) is applied to the experimental and simulated seismograms of Fig. 10 and gives us the dispersion images shown in Fig. 14. We identify three principal modes on the image of experimental dispersion over the source-relative frequency band $[0.1 - 3000Hz]$. The maxima (in black in Fig. 14) correspond to four modes: two low-velocity P-SV modes (propagation modes) at low frequency (LF) in the 0.25-1 kHz frequency band (mode 0 and 1) and two P-modes (one principal: mode 2) at higher frequencies and higher velocities in the 1.25–2.5 kHz frequency band.

The dispersion images of the numerical elastic models (2D and 3D) in Fig. 14 show clearly only two modes (mode 0 and 1). The mode 2 appears more clearly for the poroelastic model.

5 Quantitative Analysis

5.1 First Arrivals

The first-arrival (P-mode) time of the numerical data is picked at each trace and compared to both the theoretical (calculated for the unconsolidated granular medium) and experimental travel times. These travel times are shown on the time versus offset curve in Fig. 15. Computed arrival times are matching experimental and theoretical results within a 5% error range. Furthermore, the experimental first-arrival times have been picked with an error range of 5% too. Besides, an initial triggering time of approximately 0.0045s is taken into account in our comparisons as can be observed in Fig. 15 close to the source at zero-offset.

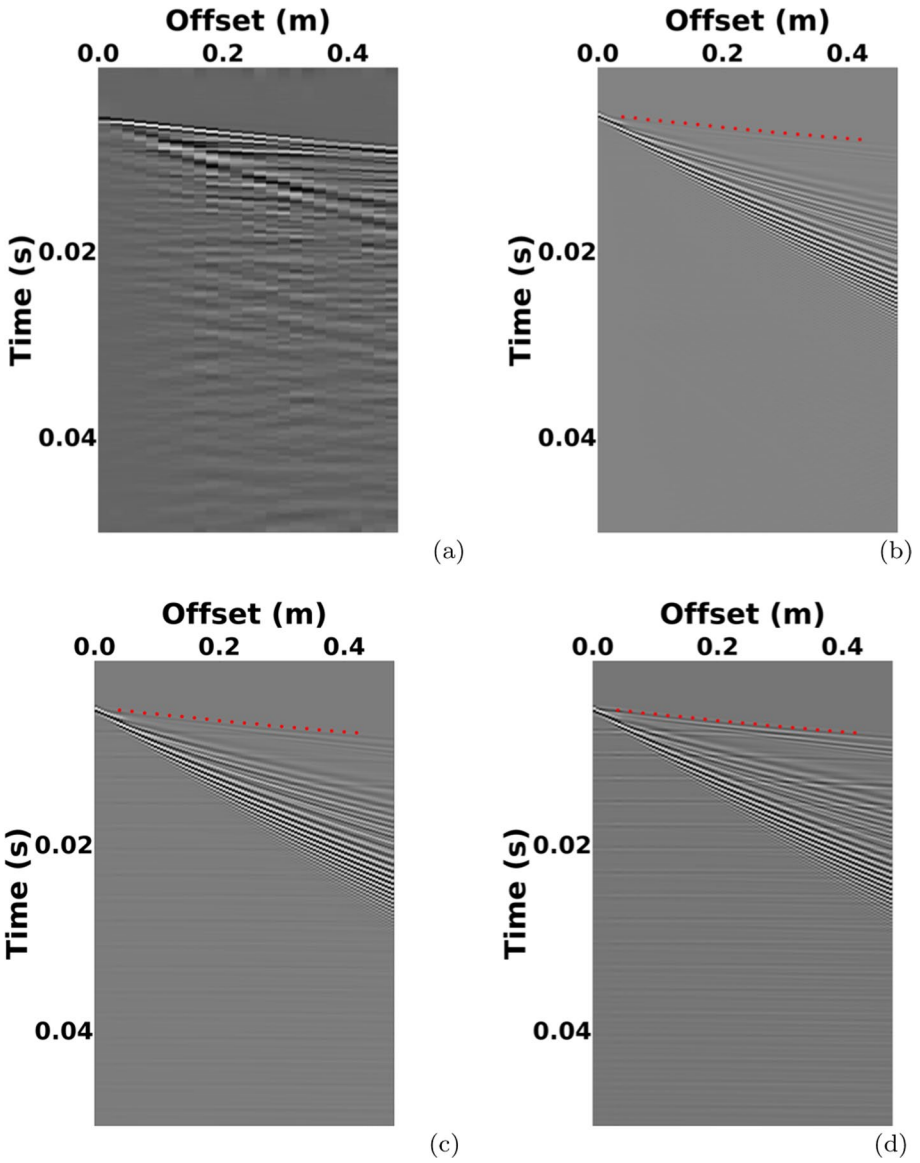

Fig. 9 Comparison between experimental filtered (**a**), 3D elastic (**b**), 2D elastic (**c**) and 2D poroelastic (**d**) seismograms (vertical component of particle velocity) in the PMLs case

Moreover, the V_p models obtained by inverting these arrival times have less than 5%–10 % errors.

5.2 Dispersion Curves

The V_s model (see equation (1-b)) is obtained by simulated annealing inversion of the fundamental mode curve extracted from the dispersion diagram of the vertical component

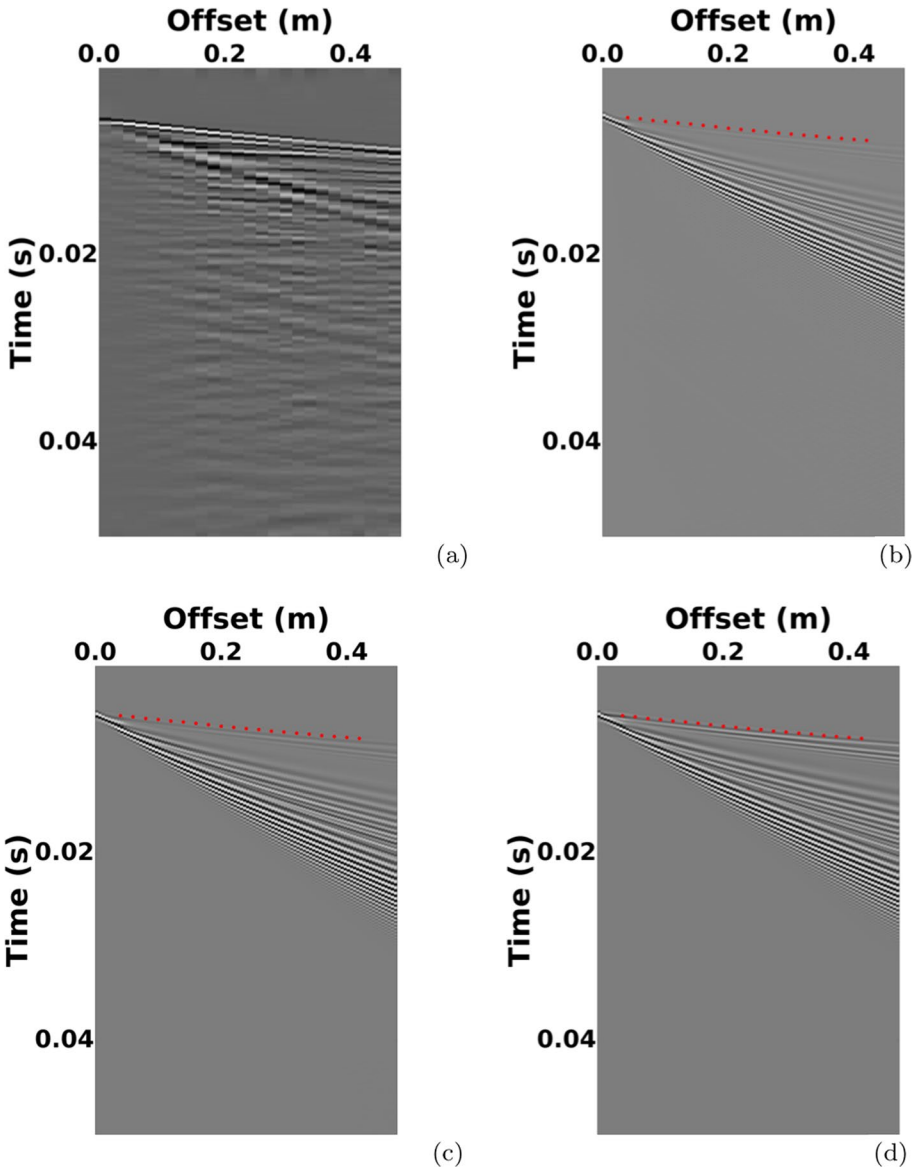

Fig. 10 Comparison between experimental filtered (**a**), 3D elastic (**b**), 2D elastic (**c**) and 2D poroelastic (**d**) seismograms (vertical component of particle velocity) in the full PMLs case

of experimental recorded signals. The V_s model has an error range of 10–15% that corresponds to 5 % data misfit error and 15% error on α_s parameter (see Bodet et al. (2014) for more details on error estimations). For this V_s model, we compute the solutions with our UNISOLVER code and the related dispersion diagrams. The dispersion curves picked for the P-SV modes identified on the dispersion images (Fig. 14) clearly fit experimental

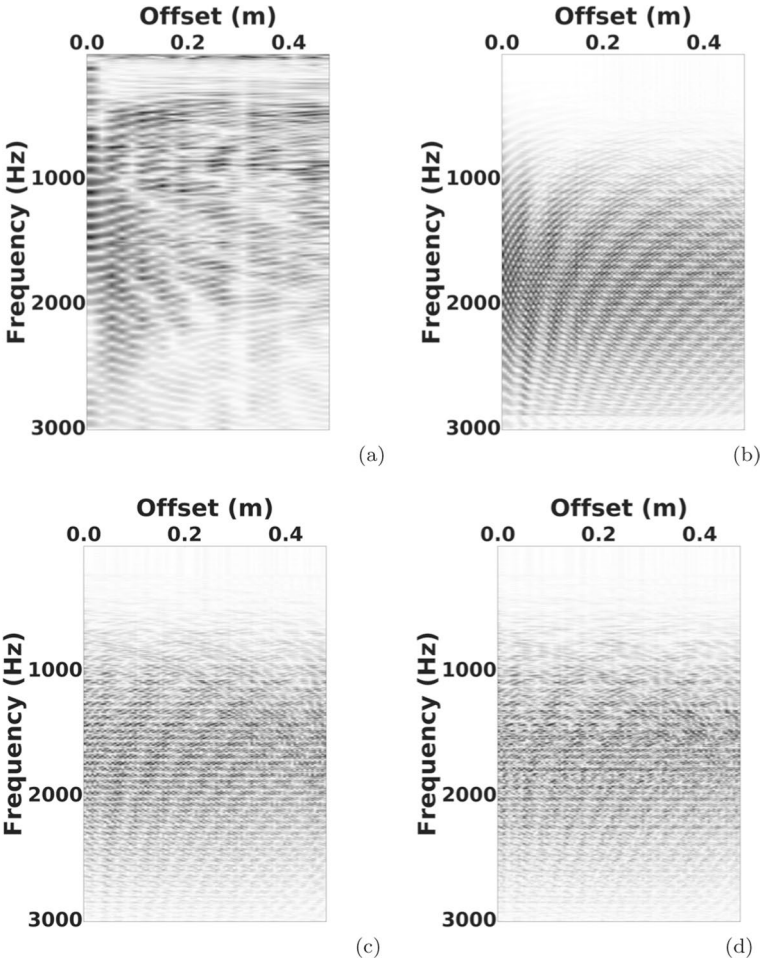

Fig. 11 Comparison between experimental (**a**), 3D elastic (**b**), 2D elastic (**c**) and 2D poroelastic (**d**) spectrograms in the Dirichlet case

and theoretical dispersion (Fig. 16). The P-SV theoretical dispersion curves are calculated using CPS/Computing Programs for Seismology (Herman et al 2013).

The P-mode picked on the 3D elastic and 2D elastic dispersion images appeared noisy due to its weak amplitude. But the P-mode picked in the 2D poroelastic case is better represented compared to experimental data and theoretical dispersion. The theoretical dispersion is computed with the CPS code that uses the Thomson–Haskell matrix propagator technique and includes the complex-valued roots of the dispersion equation. Figure 16 shows the peaks of the energy maxima corresponding to the identified modes on the dispersion images (see Fig. 14). This confirms that the modes identified on the numerical dispersion images correspond to the fundamental mode (mode 0) and to the second propagation mode (mode 1). The first *P*-mode (mode 2) is not visible enough on the dispersion image of the 3D/2D elastic model, but it appears more clearly in the poroelastic one.

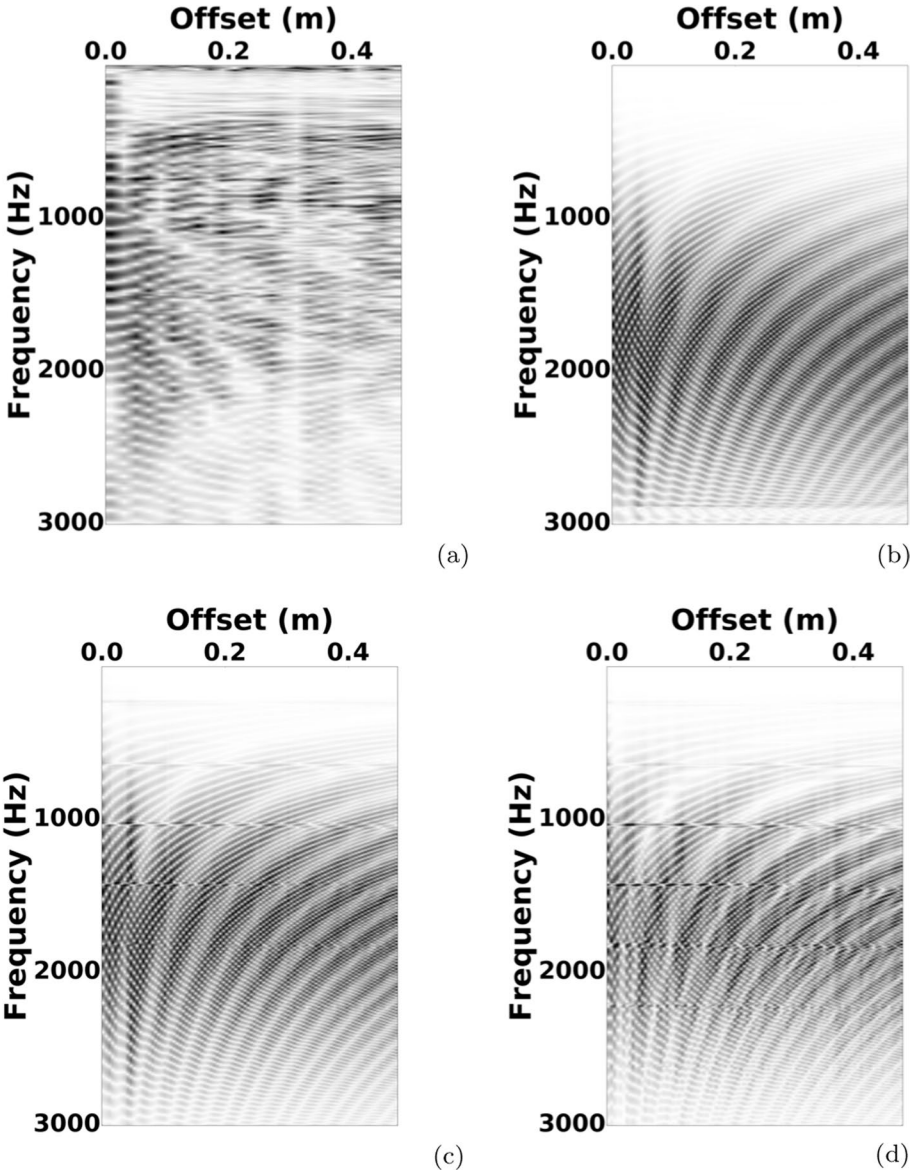

Fig. 12 Comparison between experimental (**a**), 3D elastic (**b**), 2D elastic (**c**) and 2D poroelastic (**d**) spectrograms in the PMLs case

We have been able to reproduce qualitatively the modes 0 and 1 but not the modes 2 related to *P*-modes. This is mainly due to the way the source is introduced numerically. Indeed, the way the source is modelled is crucial to detect all the main surface and P-SV modes (0, 1) as well as volumic wave modes (P-modes 2 and higher) and to better reproduce numerically the waveforms of the experimental data. The next section is devoted to this aspect and tries to bring some answers about the source modelling.

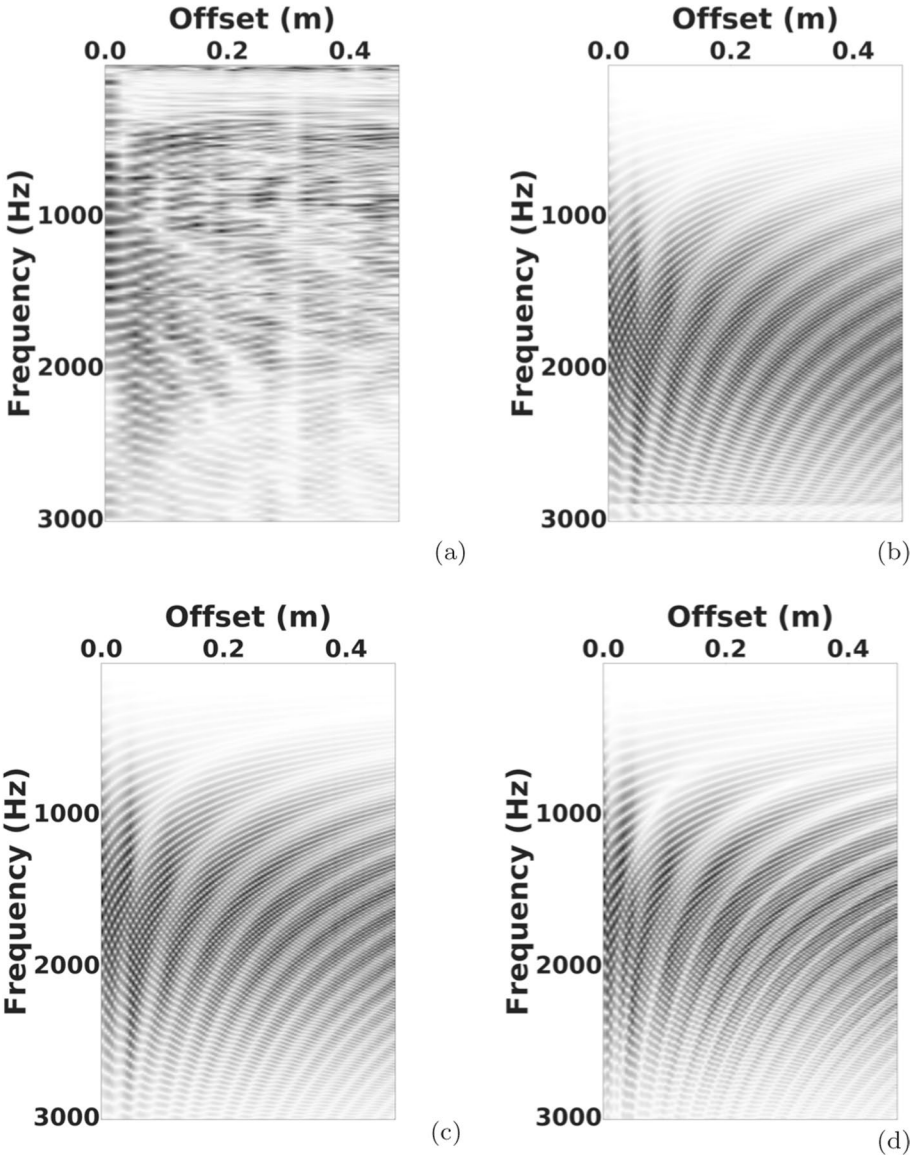

Fig. 13 Comparison between experimental (**a**), 3D elastic (**b**), 2D elastic (**c**) and 2D poroelastic (**d**) spectrograms in the full PMLs case

6 Impact of the Numerically Modelled Source

6.1 Source Configuration

Instead of considering a source defined by a stick with vibratory displacement, we consider an equivalent virtual force point source at different depths with the same inclination as the stick and the same time signal source injected during the experiment. We have considered

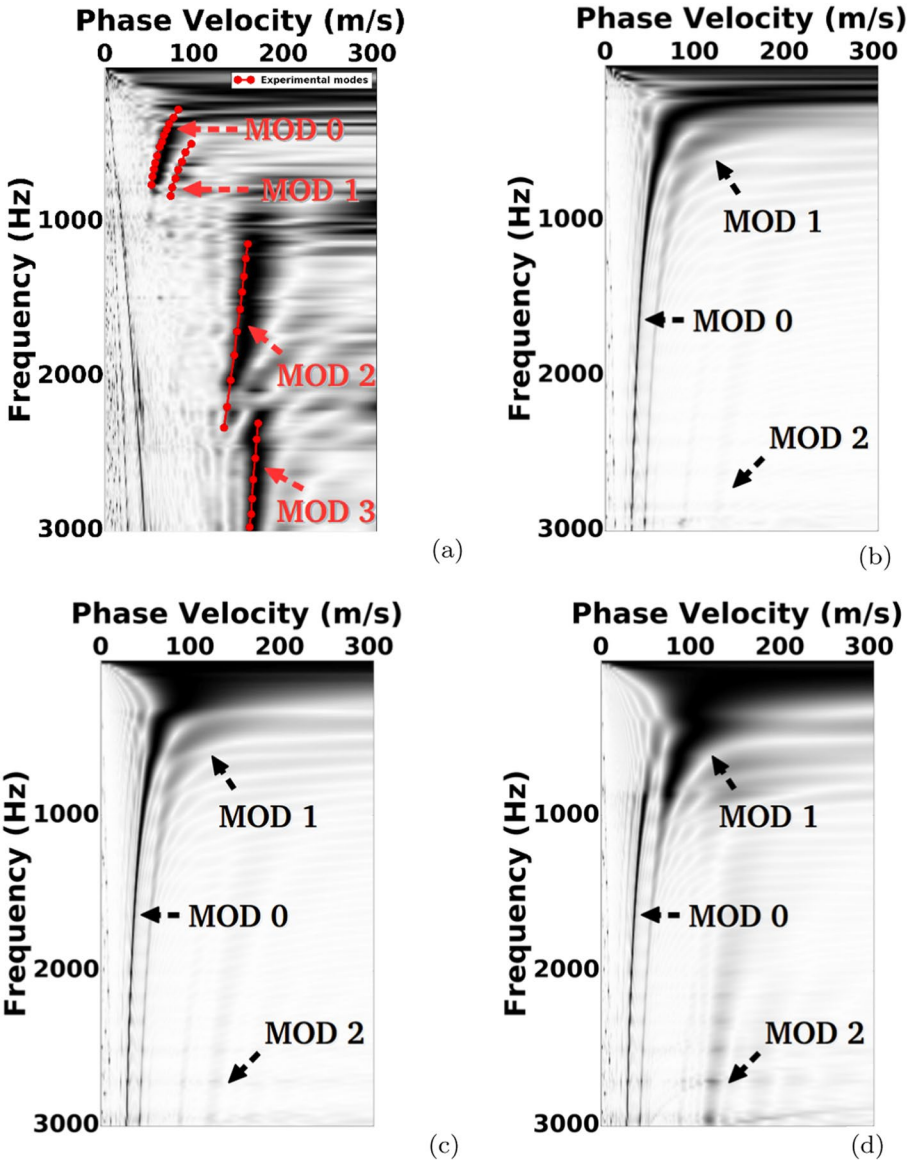

Fig. 14 Comparison between experimental filtered (**a**), 3D elastic (**b**), 2D elastic (**c**) and 2D poroelastic (**c**) dispersion images in the full PMLs case with stick source at the surface

different depths, i.e., 3.76, 4.7, 5.64, 6.58, 7.52 cm, respectively. The corresponding lengths of the stick are 4, 5, 6, 7, 8 cm, respectively (see Fig. 17). The best results are obtained in the case of a 8-cm deep source case modelled as a point source. We choose this case because better waveforms and better modes description have been obtained as discussed hereafter. For the sake of simplicity, we are not showing the related dispersion images for the other virtual source depths.

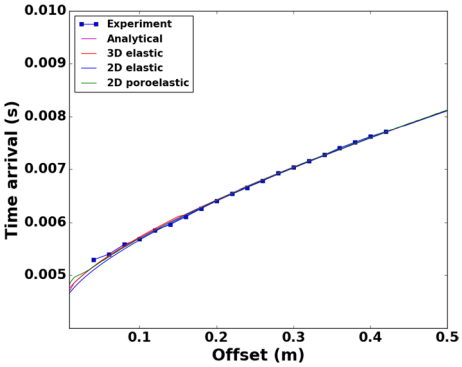

Fig. 15 First-arrival times of the 3D elastic, 2D elastic and 2D poroelastic models compared to the experimental and analytical first-arrival times

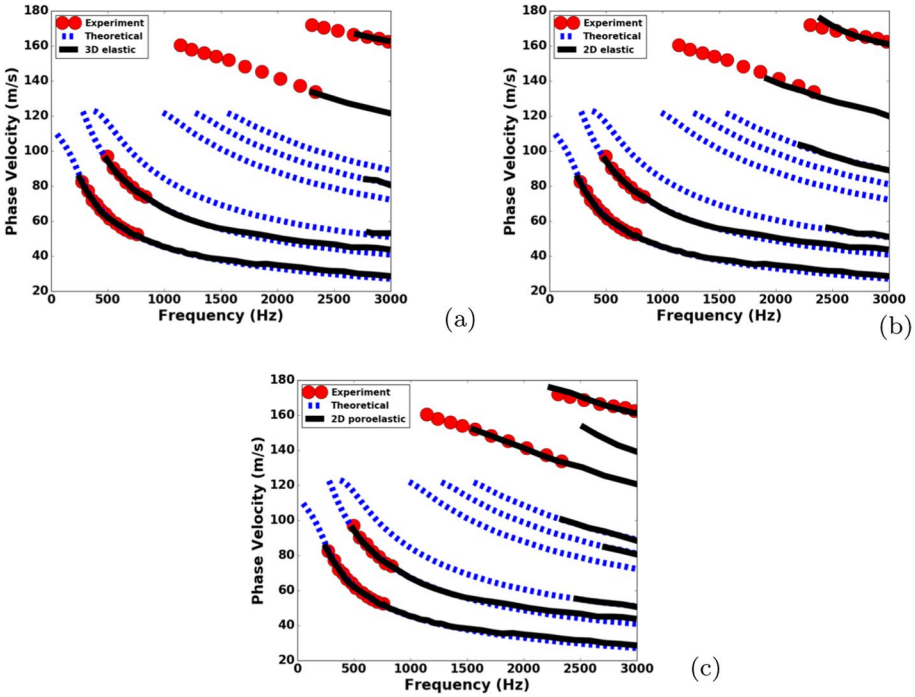

Fig. 16 Dispersion curves of 3D elastic (**a**), 2D elastic (**b**) and 2D poroelastic (**c**) seismograms compared to experimental and analytical dispersion curves with stick source at the surface

6.2 Waveforms Comparison

The numerical seismograms (2D elastic and 2D poroelastic models) in the 8-cm deep source case are more similar to the seismograms of the experiment (see Fig. 18) than the pure stick case (see Fig. 10). In Fig. 19a, b, the seismograms are scaled with offset r for receivers reasonably far (5 cm away) from the source. Quantitatively, we can see in Fig. 19a that the first wave trains of the 2D elastic and 2D poroelastic models (i.e., before $\approx 0.012\ s$)

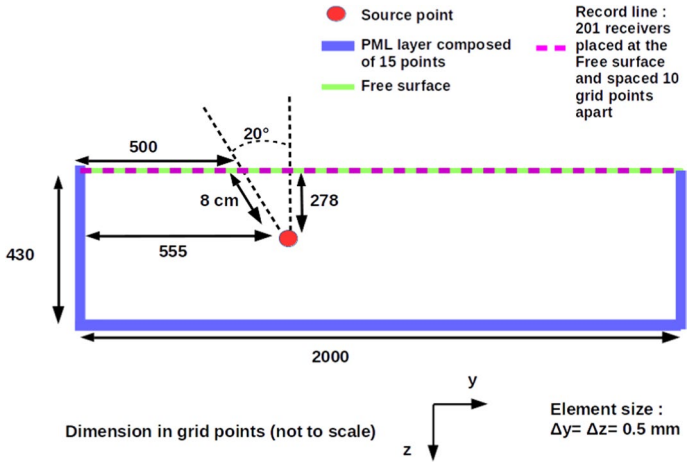

Fig. 17 Numerical setup for the 8-*cm* deep source case for the 2D elastic and 2D poroelastic model cases

are very similar to the experimental ones. However, we notice that the computed Rayleigh waveforms have overestimated amplitudes when compared to experimental surface waveforms after ≈ 0.012 *s*. On the contrary, in the 8-*cm* deep source case (Fig. 19b), the first wave train is almost superimposed to the experimental data waveform before ≈ 0.012 *s*, and the order of magnitude of the amplitudes of surface waves is similar to the amplitudes of the experimental data, which is very encouraging. The numerical modelling matches better the solution when the location of the source is deeper because the medium is better illuminated from below, between the source and the receivers, which is well known, for instance, by geophysicists working at near-surface scales in passive seismics with local earthquakes located close to the surface at a reasonable depth in the crust. Indeed, great part of the energy of the source is transmitted from below and through the shallow layers of the medium and then excite the high-frequency (small wavelength) contents of the medium. More particularly, the 2D poroelastic waveforms are matching better the real data in amplitude and phase, and more specifically the first arrivals in time and amplitude of the real data than the pure elastic waves that are more delayed in time, which can be explained by faster poroelastic V_p velocities (V_{pfast}).

In the stick source case (Fig. 19a), the amplitudes of the Rayleigh waves are very similar for both poroelastic and elastic waves, but they remain larger than the amplitudes of the surface waves present in the real data. For a 8-cm deep source (Fig. 19b), the amplitudes have decreased and are closer to those of the real data. However, the elastic waves are delayed in time with respect to the poroelastic waves in particular in the first wave train and have smaller amplitudes than poroelastic waves and real data. This can be due to faster poroelastic velocities.

As a future perspective, it would be thus important to model the source more properly in order to better reproduce the waveforms in terms of phase and amplitude. To obtain a better source, the source signal in time and space, its spatial spreading and its location at depth should be inverted. In the case of comparisons between 3D real data and 2D simulated data, a 3D-to-2D transformation should be first applied to real data through time convolution corrections and rescaling corrections depending on the offset *r*. Then, for both 2D and 3D simulations, different clusters of receivers should be considered and the real data should be

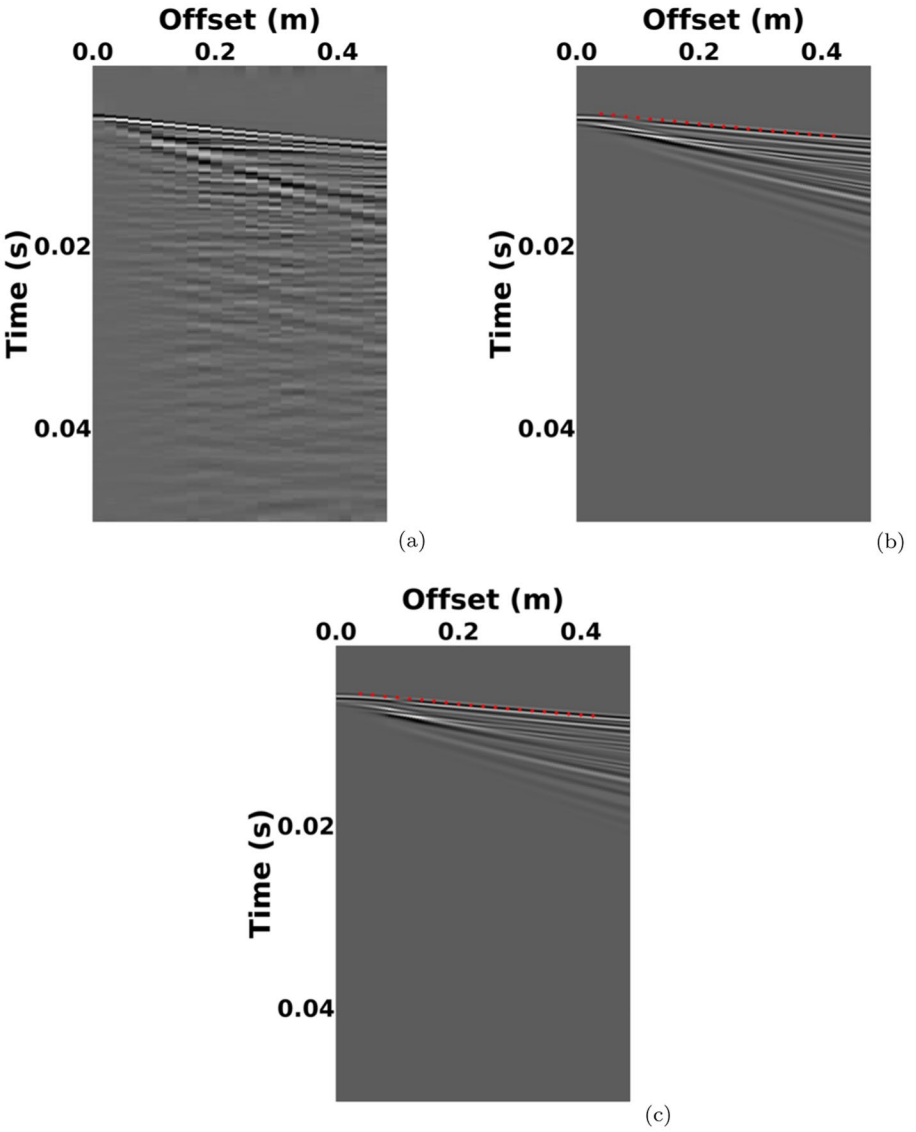

Fig. 18 Experimental filtered seismogram (**a**) compared to the 2D elastic (**b**) and 2D poroelastic (**c**) seismograms in the 8-*cm* deep source case

stacked over these clusters for signal coherency and deconvolved with the simulated data for the current model we are studying. Then, the spectral ratios of the experimental stacked data and simulated data can be used to obtain an equivalent/virtual source that explains better all the recorded waveforms in phase and amplitude. The details of building such source wavelet are well explained in Forbriger et al. (2014). The source wavelet could even be more suitably corrected by applying similar procedures as those proposed by the authors mentioned before in the data section 2.2 (Schäfer et al. 2012, 2014; Groos et al. 2013, 2014a; Forbriger et al. 2014) and more particularly when 3D-to-2D transformations are used.

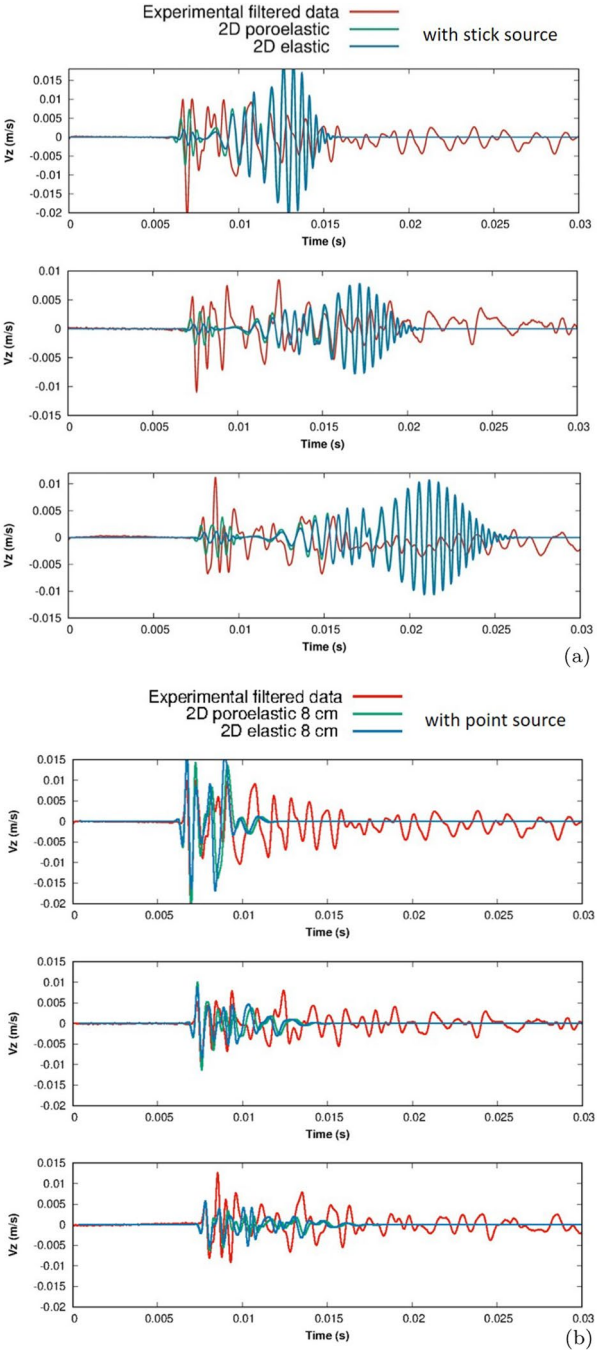

Fig. 19 **a** Comparison of the numerical seismograms (for the 2D elastic and 2D poroelastic models) with the experimental filtered ones at receivers 10, 15, and 20 in the pure (original) stick case (time in seconds). **b** Same thing but in the 8-cm deep source case. All the seismograms are zoomed over the first 30 ms because there is no signal after 25 ms in the numerical seismograms due to the PML absorbing conditions

Finally, using a multi-frequency inversion process, we could invert both the source and the recorded waveforms progressively from low to high frequencies, and this way the (poro-)elastic model as well as the source wavelet will be improved. Such source and

model inversions can be performed by using procedures similar to those also developed by Schäfer et al. (2013, 2014); Groos et al. (2013, 2014a); Forbriger et al. (2014) for near-surface applications and full-waveform inversions using efficient 3D–2D transformations to the data.

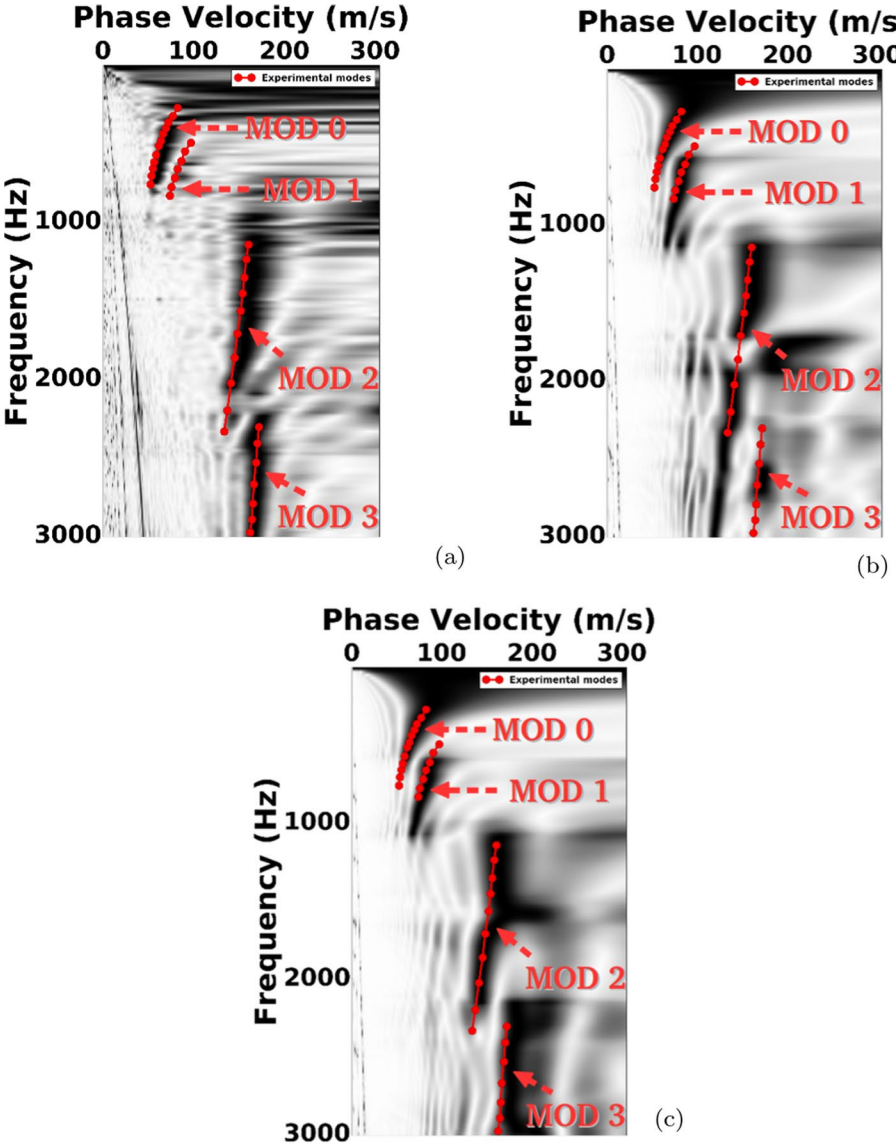

Fig. 20 Experimental dispersion image **a** compared to the 2D elastic **b** and 2D poroelastic **c** dispersion images in the 8-cm deep source case

6.3 Dispersion Analysis

In Fig. 20, we can see the very good similarity of the numerical dispersion images with the experimental one. In the previous section, the P-modes (mode 2) were not clearly reproduced in terms of amplitude. On the contrary, we obtain here the same patterns with very pronounced P-modes. These modes are very well represented in both elastic and poroelastic cases. In the poroelastic case, results are slightly improved. This can be clearly observed on the dispersion curves of Fig. 21. All these results show the crucial importance of the data sensitivity to the source modelling and particularly to the source location at depth. The deeper is the source, the more the *P*-modes can be recovered and moved towards lower frequencies. Since these *P*-modes are more pronounced, the $P-SV$ wave modes are less visible even if they are still existing but with less intensity. Of course, if the source location is too deep, surface waves will not be generated. This opens new perspectives to better define the source: inversion of its location at depth and a better spatial spreading description could be done.

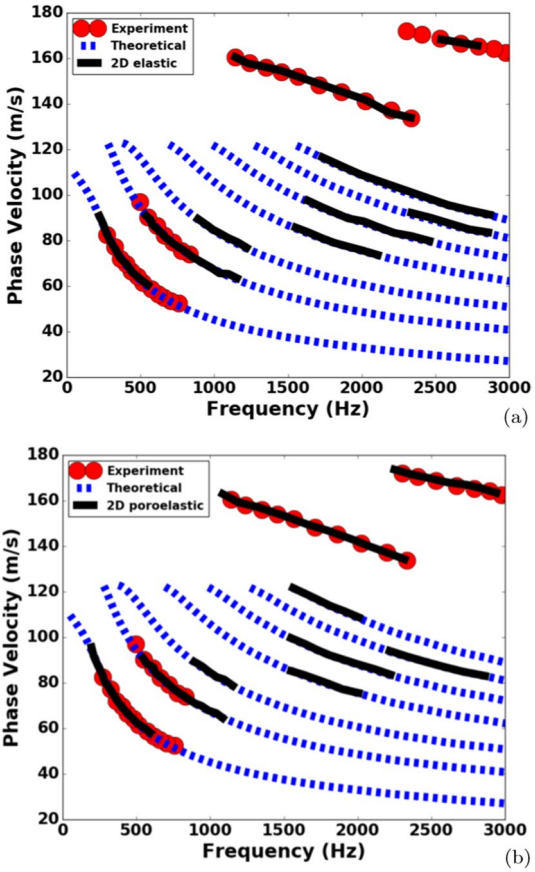

Fig. 21 Dispersion curves for the 2D elastic **a** and 2D poroelastic **b** models in the 8-cm deep source case compared to experimental and analytical dispersion curves

7 Conclusions

In this study, the V_p-V_s model has been well integrated in elastic and poroelastic codes. The results obtained from qualitative and quantitative points of view are improved compared to those presented in Bodet et al. (2014) in the case of zero overpressure, corresponding here to the dry (not fluidized) case. Numerical first arrivals and dispersion curves are very close to those of the experimental and theoretical ones.

The rheology considered (purely elastic or poroelastic) and the source location play an important role in the modelling of this kind of complex medium. Indeed, a poroelastic model combined with an acoustic source located at an adequate depth gives better results than purely elastic models and sources (a force point source or a vibratory stick) placed close to or at the surface. The fundamental mode as well as the higher modes (such as the P-modes) are better defined and are more comparable to those of the real experimental data.

The model has been validated for dry media. In future works, we plan to study fluidized media with overpressure or media partially saturated with fluids like water and to improve the models by also inverting the shape and the location of the source. A more complete study will be considered with a 3D poroelastic model, and we will also take into account attenuation effects through different viscoelastic models. This will pave the way to study gas or fluid/water detection and also to monitor some areas for CO2 storage, mitigation of flash floods, etc.

Appendix A. 3D Elastic Wave Equations

The elastodynamics equations can be formulated at the second order in displacement as:

$$\rho \frac{\partial^2 u_i}{\partial t^2} = \partial_j \sigma_{ij} + s_i,$$
$$\epsilon_{ij} = \frac{1}{2}\left(u_{i,j} + u_{j,i}\right),$$
$$\sigma_{ij} = \lambda \delta_{ij} \epsilon_{kk} + 2\mu \epsilon_{ij}.$$

However, the first-order formulation (velocity-stress) of the 3D elastic wave equations for a linear, isotropic medium submitted to external forces is given by Graves (1996):

$$
\begin{aligned}
\rho\frac{\partial v_x}{\partial t} &= \frac{\partial \sigma_{xx}}{\partial x} + \frac{\partial \sigma_{xy}}{\partial y} + \frac{\partial \sigma_{xz}}{\partial z} + s_x,\\
\rho\frac{\partial v_y}{\partial t} &= \frac{\partial \sigma_{xy}}{\partial x} + \frac{\partial \sigma_{yy}}{\partial y} + \frac{\partial \sigma_{yz}}{\partial z} + s_y,\\
\rho\frac{\partial v_z}{\partial t} &= \frac{\partial \sigma_{xz}}{\partial x} + \frac{\partial \sigma_{yz}}{\partial y} + \frac{\partial \sigma_{zz}}{\partial z} + s_z,\\
\frac{\partial \sigma_{xx}}{\partial t} &= (\lambda+2\mu)\frac{\partial v_x}{\partial x} + \lambda\left(\frac{\partial v_y}{\partial y} + \frac{\partial v_z}{\partial z}\right),\\
\frac{\partial \sigma_{yy}}{\partial t} &= (\lambda+2\mu)\frac{\partial v_y}{\partial y} + \lambda\left(\frac{\partial v_x}{\partial x} + \frac{\partial v_z}{\partial z}\right),\\
\frac{\partial \sigma_{zz}}{\partial t} &= (\lambda+2\mu)\frac{\partial v_z}{\partial z} + \lambda\left(\frac{\partial v_x}{\partial x} + \frac{\partial v_z}{\partial z}\right),\\
\frac{\partial \sigma_{xy}}{\partial t} &= \mu\left(\frac{\partial v_y}{\partial x} + \frac{\partial v_x}{\partial y}\right),\\
\frac{\partial \sigma_{xz}}{\partial t} &= \mu\left(\frac{\partial v_z}{\partial x} + \frac{\partial v_x}{\partial z}\right),\\
\frac{\partial \sigma_{yz}}{\partial t} &= \mu\left(\frac{\partial v_z}{\partial y} + \frac{\partial v_y}{\partial z}\right).
\end{aligned}
\tag{2}
$$

In these equations, v_x, v_y, v_z are the velocity components; σ_{xx}, σ_{yy}, σ_{zz}, σ_{xy}, σ_{xz}, σ_{yz} are the stress components; s_x, s_y, s_z are the body-force components; ρ is the density; λ and μ are Lamé parameters.

Appendix B. 2D Elastic Wave Equations

In the 2D particular case, 2D elastic wave equations for an isotropic medium submitted to external forces can be written using a velocity-stress formulation such as the following linear and hyperbolic system (Dumbser and Käser 2006):

$$
\begin{aligned}
\rho\frac{\partial v_x}{\partial t} &= \frac{\partial \sigma_{xx}}{\partial x} + \frac{\partial \sigma_{xz}}{\partial z} + s_x,\\
\rho\frac{\partial v_z}{\partial t} &= \frac{\partial \sigma_{xz}}{\partial x} + \frac{\partial \sigma_{zz}}{\partial z} + s_z,\\
\frac{\partial \sigma_{xx}}{\partial t} &= (\lambda+2\mu)\frac{\partial v_x}{\partial x} + \lambda\frac{\partial v_z}{\partial z},\\
\frac{\partial \sigma_{zz}}{\partial t} &= (\lambda+2\mu)\frac{\partial v_z}{\partial z} + \lambda\frac{\partial v_x}{\partial x},\\
\frac{\partial \sigma_{xz}}{\partial t} &= \mu\left(\frac{\partial v_z}{\partial x} + \frac{\partial v_x}{\partial z}\right),
\end{aligned}
\tag{3}
$$

where λ and μ are Lamé parameters, ρ is the density, and s_x and s_z are the space-dependent source terms in x and z directions. The compressional stress components are given by σ_{xx} and σ_{zz}, and the shear stress is σ_{xz}. The components of particle velocities in direction x and z are denoted by v_x and v_z, respectively.

Appendix C. 2D Poroelastic Wave Equations

Porous materials are made of a solid phase (called the frame) and of a fluid phase and can be considered as an interconnected network of pores inside the solid (Pride et al. 2004). When a fluid flow is able to cause the solid to deform, the material is called poroelastic. Unconsolidated granular media can be seen as a poroelastic material in which air or water can play the role of the fluid and grains the solid. Poroelastic materials are most of the time modelled using the Biot theory (Biot (1956a) and Biot (1956b)). The differential or "strong" formulation of the poroelastic wave equations can be written as (Carcione 2007), (Carcione 2014):

$$\rho\partial_t^2 u^s + \rho_f \partial_t^2 w = \nabla.\big(C : \nabla u^s - \alpha P^f I\big), \tag{4}$$

$$\rho_f \partial_t^2 u^s + \rho_w \partial_t^2 w = -\nabla P^f - K\partial_t w, \tag{5}$$

$$P^f = -\alpha M \nabla.u^s - M\nabla.w, \tag{6}$$

where $u^s = (u_i^s)_{i=1,2}$, $w = \Phi\big(u^f - u^s\big)$ and $u^f = (u_i^f)_{i=1,2}$ are, respectively, the solid, relative, and fluid displacement vectors; Φ is the porosity; and C is the stiffness tensor of the isotropic elastic solid matrix, defined as:

$$\sigma_{ij}^s = (C : \epsilon)_{ij} = \lambda_s \delta_{ij}\epsilon_{kk} + 2\mu\epsilon_{ij}, \tag{7}$$

$$\epsilon_{ij} = \frac{1}{2}\left(\frac{\partial u_i^s}{\partial x_j} + \frac{\partial u_j^s}{\partial x_i}\right), \tag{8}$$

$$P^f = -\alpha M \nabla.u^s - M\nabla.w, \tag{9}$$

where indices i and j can be here 1 or 2 in $2D$ and with the Einstein convention of implicit summation over a repeated index. P^f is the pressure in the fluid. σ^s and ϵ are, respectively, the stress and strain tensors of the isotropic elastic solid frame. The stress tensor of the fluid-filled solid matrix is $\sigma = \sigma^s - \alpha P^f I$, and $\rho = \Phi\rho_f + (1-\Phi)\rho_s$ is the density of the saturated medium, where ρ_s and ρ_f are the solid and fluid densities, respectively. The apparent density is $\rho_w = a\frac{\rho_f}{\Phi}$ where a denotes the tortuosity. The shear modulus is μ and $\lambda_s = \lambda - \alpha^2 M$ is the Lamé coefficient in the solid matrix, where λ is the Lamé coefficient of the saturated matrix. The α and M variables are functions of the porosity and bulk moduli of the fluid and solid components of the porous medium and are given by the following expressions:

$$\alpha = 1 - \frac{K_{fr}}{K_s}, \tag{10}$$

$$M = 1/\big[\Phi/K_f + (\Phi - \alpha)/K_s\big], \tag{11}$$

where K_{fr} is the incompressibility modulus of the porous frame, K_s is the incompressibility modulus of the solid matrix, and K_f is the incompressibility modulus of the fluid. The viscous damping coefficient is:

$$K = \kappa/\eta, \tag{12}$$

where κ is the permeability of the solid matrix and η is the fluid viscosity. Equations (4) to (7) can be written using a first-order velocity-stress formulation:

$$\left(\rho_w \rho - \rho_f^2\right)\partial_t v^s = \rho_w \nabla.\sigma + \rho_f \nabla P^f + \rho K v^f, \tag{13}$$

$$\left(\rho_w \rho - \rho_f^2\right)\partial_t v^f = -\rho_f \nabla.\sigma - \rho \nabla P^f - \rho_f K v^f, \tag{14}$$

$$\partial_t \sigma = C : \nabla v^s - \alpha \partial_t P^f I, \tag{15}$$

$$\partial_t P^f = -\alpha M \nabla.v^s - M \nabla.v^f, \tag{16}$$

where $v^s = (v_i^s)_{i=1,2}$ and $v^f = \partial_t w = (v_i^f)_{i=1,2}$ are the solid and filtration velocity vectors, respectively. σ is the effective stress tensor of the porous medium. As in Zeng and Liu (2001), using the trace of the strain tensor $Tr(\epsilon) = \epsilon_{ii}$ and an auxiliary variable ξ, we rewrite the system as:

$$\left(\rho_w \rho - \rho_f^2\right)\partial_t v_i^s = \rho_w \partial_j \sigma_{ij} + \rho_f \partial_i P^f + \rho K v_i^f, \tag{17}$$

$$\left(\rho_w \rho - \rho_f^2\right)\partial_t v_i^f = -\rho_f \partial_j \sigma_{ij} - \rho \partial_i P^f - \rho_f K v_i^f, \tag{18}$$

$$\epsilon_{ij} = \frac{1}{2}\left(\partial_j v_i^s + \partial_i v_j^s\right), \tag{19}$$

$$\partial_t \xi = -\partial_i v_i^f, \tag{20}$$

$$P^f = -\alpha M Tr(\epsilon) + M\xi, \tag{21}$$

$$\sigma_{ij}^s = \lambda^s \delta_{ij} Tr(\epsilon) + 2\mu \epsilon_{ij}, \tag{22}$$

$$\sigma_{ij} = \sigma_{ij}^s - \alpha P^f \delta_{ij}. \tag{23}$$

This system of equations has seven wave eigenvalues related to seven wave velocity modes (instead of five for the elastic case). Those wave velocities are $\pm V_{pFAST}$, $\pm V_{pSLOW}$, $\pm V_s$ and 0. The shear velocity V_s and the fast and slow P-wave velocities (V_{pFAST} and V_{pSLOW}) can be expressed as (Sidler et al. 2014):

$$V_s = \sqrt{\frac{\mu}{a_1}}, \tag{24}$$

$$V_{pFAST} = \sqrt{\frac{-b_1 + \sqrt{\Delta}}{2a_1}}, \tag{25}$$

$$V_{pSLOW} = \sqrt{\frac{-b_1 - \sqrt{\Delta}}{2a_1}}, \tag{26}$$

where

$a_1 = \rho_{11}\rho_{22} - \rho_{12}^2$,
$b_1 = -S\rho_{22} - R\rho_{11} + 2ga\rho_{11}$,
$c_1 = SR - ga^2$,
$\rho_{11} = \rho + \rho_f\Phi(a-2)$,
$\rho_{12} = \Phi\rho_f(1-a)$,
$\rho_{22} = a\rho_f\Phi$,
$S = \lambda + 2\mu$,
$R = M\Phi^2$,
$\Delta = b_1^2 - 4a_1c_1$,
$ga = M\Phi(\alpha - \Phi)$.

In Table 1, a summary of the different parameters of the poroelastic model is provided.

Biot's characteristic frequency f_c defines the transition between two poroelastic regimes (with or without attenuation) and is given as follows (see Biot 1956b; Carcione 2007 and Morency and Tromp 2008):

$$f_c = \min\left(\frac{\eta\Phi}{2\pi a\rho_f\kappa}\right), \tag{27}$$

see parameters in Table 1.

In our study, the maximum frequency range f_{max} of the source is such that $f_{max} < f_c$. Therefore, in the experimental and numerical modelling of unconsolidated granular media under study, we choose to stay in the poroelastic regime without attenuation.

Table 1 Parameters of the poroelastic model

Parameters of the poroelastic model	
Φ	Porosity
ρ	Density of the saturated medium
ρ_s	Density of the solid
ρ_f	Density of the fluid
ρ_w	Apparent density
K_s	Incompressibility modulus of the solid matrix
K_f	Incompressibility modulus of the fluid
K_{fr}	Incompressibility modulus of the porous frame
κ	Permeability of the solid matrix
η	Fluid viscosity
a	Tortuosity
λ	Lamé coefficient of the saturated matrix
λ_s	Lamé coefficient in the solid matrix
μ	Shear modulus

Appendix D. Performance of UNISOLVER Parallel Code

The fourth-order 3D UNISOLVER parallel code has been scaled over different numbers of processors (up to 400) of Olympe supercomputer at CALMIP computing centre of Toulouse (France) by using MPI (Message-Passing-Interface) library. The computational domain has been cut along the longitudinal y-axis (from 20 points down to 5 grid points per processor along the y-axis). A buffer overlapping corresponding to two grid points between subdomains (one subdomain per processor) is used to communicate the particle velocities and stresses and material properties between processors via 'MPI_Send' and 'MPI_Recv' communication operations. As we can see in Fig. 22, the strong scaling obtained by measuring the CPU time versus the number of processors is very satisfactory, despite the use of blocking communication operations. This strategy is classical (see (Komatitsch and Martin 2007)).

We underline that asynchronous iterative schemes of computation which cover communications by computations in the inner subdomains as depicted in Miellou et al. 1998; El Baz et al. 2001; Chau et al. 2007; El Baz et al. 2005; Martin et al. 2008a are also very efficient.

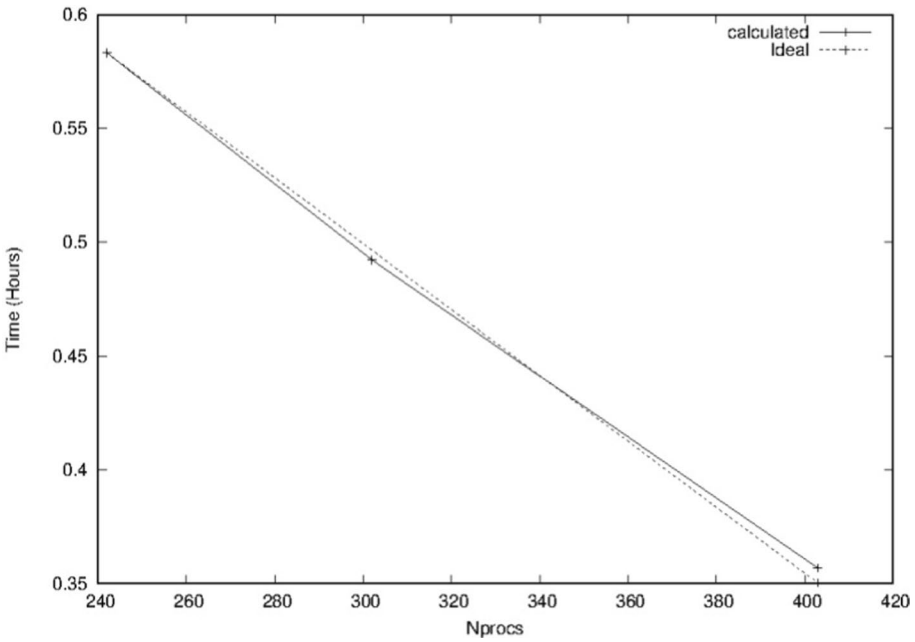

Fig. 22 Strong scaling of the UNISOLVER code over 200 up to 400 processors on Olympe supercomputer. Ideal and numerical tests scaling curves are shown

Acknowledgements The authors thank the Université Fédérale de Toulouse Midi-Pyrénées (UFT-MIP) and Occitanie Region Research Council under DIMSCALE3D project, the CALMIP mesocentre in Toulouse, France, under supercomputing project $P1135-2021A$ and $P1135-2022A$, and computing platform

NUWA of the OMP/Observatoire Midi-Pyrénées, France. The authors thank the reviewers for their very useful suggestions and remarks to improve the manuscript.

Declarations

Conflict of interest All authors declare that they have no conflict of interest.

Ethical approval This article does not contain any studies with human participants or animals performed by any of the authors.

References

Bachrach R, Dvorkin J, Nur A (1998) High-resolution shallow-seismic experiments in sand, part ii: velocities in shallow unconsolidated sand. Geophysics 63(4):1234–1240

Bergamo P, Bodet L, Socco LV, Mourgues R, Tournat V (2014) Physical modelling of a surface-wave survey over a laterally varying granular medium with property contrasts and velocity gradients. Geophys J Int doi 10(1121/1):4712020

Biot MA (1956) Theory of propagation of elastic waves in a fluid-saturated porous solid. I: low-frequency range. J Acoust Soc Am 28:168–178

Biot MA (1956) Theory of propagation of elastic waves in a fluid-saturated porous solid. II: higher-frequency range. J Acoust Soc Am 28:179–191

Bitri A, Grandjean G, Baltassat J (2002) Caractérisation du proche sous-sol le long de tracés linéaires par profilage sasw. In: In Journées AGAP, LCPC, pp 503-506

Bodet L, Jacob X, Tournat V, Mourgues R, Gusev V (2010) Elasticity profile of an unconsolidated granular medium inferred from guided waves: toward acoustic monitoring of analogue models. Tectonophysics 496:99–104

Bodet L, Dhemaied A, Martin R, Mourgues R, Rejiba F, Tournat V (2014) Small-scale physical modeling of seismic-wave propagation using unconsolidated granular media. Geophysics 79(6):T323–T339

Carcione JM (2007) Wave fields in real media: theory and numerical simulation of wave propagation in anisotropic, anelastic, porous and electromagnetic media, 2nd edn. Elsevier Science, Amsterdam, The Netherlands

Carcione JM (2014) Wave fields in real media: wave propagation in anisotropic. Anelastic, Elsevier, Porous and Electromagnetic Media

Chau M, El Baz D, Guivarch R, Spiteri P (2007) MPI implementation of parallel subdomain methods for linear and nonlinear convection-diffusion problems. J Parallel Distrib Comput 67(5):581–591

Dumbser M, Käser M (2006) An arbitrary high-order discontinuous Galerkin method for elastic waves on unstructured meshes-II. The three-dimensional isotropic case. Geophys J Int 167(1):319–336. https://doi.org/10.1111/j.1365-246X.2006.03120.x

El Baz D, Miellou J, Spiteri P (2001) Asynchronous schwarz alternating methods with flexible communication for the obstacle problem. Calculateurs Parallèles, Réseaux et Systmes Répartis 13(01):47–66

El Baz D, Frommer A, Spiteri P (2005) Asynchronous iterations with flexible communication: contracting operators. J Comput Appl Math 176:91–103

Forbriger T, Groos L, Schäfer M (2014) Line-source simulation for shallow-seismic data. Part 1: theoretical background. Geophys J Int 198(3):1387–1404

Foti S (2000) Multistation method for geotecnical characterization using surface waves. PhD thesis, Politechnico di Torino, Italy

Ganji V, Gucunski N, Maher A (1997) Detection of underground obsacles by sasw method - numerical aspects. J Geotech Geoenviron Eng 123:212–219

Gassmann F (1951) Elastic waves through a packing of spheres. Geophysics 16(4):673–685

Graves RW (1996) Simulating seismic wave propagation in 3D elastic media using staggered-grid finite differences. Bull Seismol Soc Am 86(4):1091–1106

Groos L, Schäfer M, Forbriger T, Bohlen T (2013) Comparison of 1d conventional and 2d full waveform inversion of recorded shallow seismic rayleigh waves 10.3997/2214-4609.20131337

Groos L, Schäfer M, Butzer S, Forbriger T, Bohlen T (2014a) Challenges for 2-d elastic full waveform inversion of shallow-seismic rayleigh waves 10.3997/2214-4609.20140532

Groos L, Schäfer M, Forbriger T, Bohlen T (2014) The role of attenuation in 2d full-waveform inversion of shallow-seismic body and rayleigh waves. Geophysics 79(6):R247–R261. https://doi.org/10.1190/geo2013-0462.1

Improta L, Zollo A, Herrero A, Frattini R, Virieux J, Dell Aversana P (2002) Seismic imaging of complex structures by non-linear traveltime inversion of dense wide-angle data?: application to a thrust belt. Geophys J Int 151:264–278

Jacob X, Aleshin V, Tournat V, Leclaire P, Lauriks W, Gusev V (2008) Acoustic probing of the jamming transition in an unconsolidated granular medium. Phys Rev Lett 100(15):158003

Komatitsch D (1997) Méthodes spectrales et éléments spectraux pour l'équation de l'élastodynamique 2D et 3D en milieu hétérogène (Spectral and spectral-element methods for the 2D and 3D elastodynamics equations in heterogeneous media). PhD thesis, Institut de Physique du Globe, Paris, France, p 187

Komatitsch D, Martin R (2007) An unsplit convolutional Perfectly Matched Layer improved at grazing incidence for the seismic wave equation. Geophysics 72(5):SM155–SM167. https://doi.org/10.1190/1.2757586

Le Meur H (1994) Tomographie tridimensionnelle à partir des temps des premières arrivés des ondes p et s. application á la rǵion de patras (grèce). PhD thesis, Université de Paris VII, Paris, France

Makse HA, Gland N, Johnson DL, Schwartz LM (1999) Why effective medium theory fails in granular materials. Phys Rev Lett 83(24):5070

Martin R, Komatitsch D (2009) An unsplit convolutional perfectly matched layer technique improved at grazing incidence for the viscoelastic wave equation. Geophys J Int 179(1):333–344. https://doi.org/10.1111/j.1365-246X.2009.04278.x

Martin R, Komatitsch D, Blitz C, Le Goff N (2008) Simulation of seismic wave propagation in an asteroid based upon an unstructured MPI spectral-element method: blocking and non-blocking communication strategies. Lect Notes Comput Sci 5336:350–363

Martin R, Komatitsch D, Ezziani A (2008) An unsplit convolutional perfectly matched layer improved at grazing incidence for seismic wave equation in poroelastic media. Geophysics 73(4):T51–T61. https://doi.org/10.1190/1.2939484

Martin R, Komatitsch D, Gedney SD, Bruthiaux E (2010) A high-order time and space formulation of the unsplit perfectly matched layer for the seismic wave equation using Auxiliary Differential Equations (ADE-PML). Comput Model Eng Sci 56(1):17–42

Miellou J, El Baz D, Spiteri P (1998) A new class of asynchronous iterative methods with order intervals. Math Comput 67(01):237–255. https://doi.org/10.1090/S0025-5718-98-00885-0

Moczo P, Bystrický E, Kristek J, Carcione JM, Bouchon M (1997) Hybrid modeling of P-SV seismic motion at inhomogeneous viscoelastic topographic structures. Bull Seismol Soc Am 87:1305–1323

Moczo P, Kristek J, Bystrický E (2001) Efficiency and optimization of the 3-D finite-difference modeling of seismic ground motion. J Comput Acoust 9(2):593–609

Moczo P, Kristek J, Galis M, Pazak P (2010) On accuracy of the finite-difference and finite-element schemes with respect to p-wave to s-wave speed ratio. Geophys J Int 182(1):493–510

Morency C, Tromp J (2008) Spectral-element simulations of wave propagation in porous media. Geophys J Int 175:301–345. https://doi.org/10.1111/j.1365-246X.2008.03907.x

Morency C, Luo Y, Tromp J (2009) Finite-frequency kernels for wave propagation in porous media based upon adjoint methods. Geophys J Int 179:1148–1168. https://doi.org/10.1111/j.1365-246X.2009.04332

Nazarian S, Stokoe K (1984) In situ shear wave velocities from spectral analysis of surface waves. Proc 8th Conf Earthquake Eng Nice France 3:31–38

Palermo A, Krödel S, Matlack KH, Zaccherini R, Dertimanis VK, Chatzi EN, Marzani A, Daraio C (2018) Hybridization of guided surface acoustic modes in unconsolidated granular media by a resonant metasurface. Phys Rev Appl 9:054026. https://doi.org/10.1103/PhysRevApplied.9.054026

Park S, Elrick S (1998) Predictions of shear-wave velocities in southern California using surface geology. Bullet Seism Soc Am 88(3):677–685

Pasquet S, Bodet L (2017) Swip: an integrated workflow for surface-wave dispersion inversion and profiling. Geophysics 82(6):WB47–WB61

Pride SR, Berryman JG, Harris JM (2004) Seismic attenuation due to wave-induced flow. J Geophys Res 109:681–693

Pu X, Palermo A, Cheng Z, Shi Z, Marzani A (2020) Seismic metasurfaces on porous layered media: surface resonators and fluid-solid interaction effects on the propagation of rayleigh waves. Int J Eng Sci 154:103347. https://doi.org/10.1016/j.ijengsci.2020.103347

Ravaut C (2003) Tomographie sismique haute résolution de la croûte terrestre : inversion combiné des temps de trajet et des formes d'ondes de données sismiques réflexion/réfraction grand angle multitraces. PhD thesis, Université de Nice Sophia Antipolis, Nice, France

Schäfer M, Groos L, Forbriger T, Bohlen T (2012) On the effects of geometrical spreading corrections for a 2d full waveform inversion of recorded shallow seismic surface waves. 10.3997/2214-4609.20148327

Schäfer M, Groos L, Forbriger T, Bohlen T (2013) 2D full waveform inversion of recorded shallow seismic rayleigh waves on a significantly 2d structure. Near Surf Geosci. https://doi.org/10.3997/2214-4609.20131338

Schäfer M, Groos L, Forbriger T, Bohlen T (2014) Line-source simulation for shallow-seismic data. part 2: full-waveform inversion-a synthetic 2-d case study. Geophys J Int 198:1405–1418. https://doi.org/10.1093/gji/ggu171

Schön JH (2015) Physical properties of rocks: Fundamentals and principles of petrophysics. Elsevier

Sidler R, Carcione JM, Holliger K (2014) A pseudospectral method for the simulation of 3-D ultrasonic and seismic waves in heterogeneous poroelastic borehole environments. Geophys J Int 196(2):1134–1151

Tournat V, Gusev V (2010) Acoustics of unconsolidated "model" granular media: An overview of recent results and several open problems. Acta Acust United Acust 96(2):208–224

Xia J (2014) Estimation of near-surface shear-wave velocities and quality factors using multichannel analysis of surface-wave methods. J Appl Geophys 103:140–151

Xia J, Miller R, Park C (1999) Estimation of near-surface shear-wave velocity by inversion of rayleigh waves. Geophysics 64(3):691–700

Zaccherini R, Palermo A, Marzani A, Colombi A, Dertimanis V, Chatzi E (2020) Mitigation of rayleigh-like waves in granular media via multi-layer resonant metabarriers. Appl Phys Lett 117(25):254103. https://doi.org/10.1063/5.0031113

Zelt C, Smith R (1992) Seismic traveltime inversion for 2d crustal velocity structure. Geophys J Int 108:16–34

Zeng YQ, Liu QH (2001) A staggered-grid finite-difference method with perfectly matched layers for poroelastic wave equations. J Acoust Soc Am 109(6):2571–2580. https://doi.org/10.1121/1.1369783

Zimmer MA, Prasad M, Mavko G, Nur A (2007) Seismic velocities of unconsolidated sands: Part 1-pressure trends from 0.1 to 20 mpa. Geophysics 72(1):E1–E13

Publisher's Note Springer Nature remains neutral with regard to jurisdictional claims in published maps and institutional affiliations.

Springer Nature or its licensor (e.g. a society or other partner) holds exclusive rights to this article under a publishing agreement with the author(s) or other rightsholder(s); author self-archiving of the accepted manuscript version of this article is solely governed by the terms of such publishing agreement and applicable law.

Authors and Affiliations

K. Asfour[1] · R. Martin[1] · D. El Baz[2] · L. Bodet[3] · B. Plazolles[1]

✉ R. Martin
roland.martin@get.omp.eu

K. Asfour
Kassem.Asfour@hotmail.com

D. El Baz
elbaz@laas.fr

L. Bodet
ludovic.bodet@sorbonne-universite.fr

B. Plazolles
bastien.plazolles@get.omp.eu

[1] Laboratoire GET, Université Toulouse 3 Paul Sabatier, IRD, CNRS UMR 5563, 31400 Toulouse, France

[2] LAAS-CNRS, Université de Toulouse, UPR 8001, 31031 Toulouse, France

[3] Sorbonne Université, CNRS, EPHE, UMR 7619 METIS, 75252 Paris Cedex 5, France